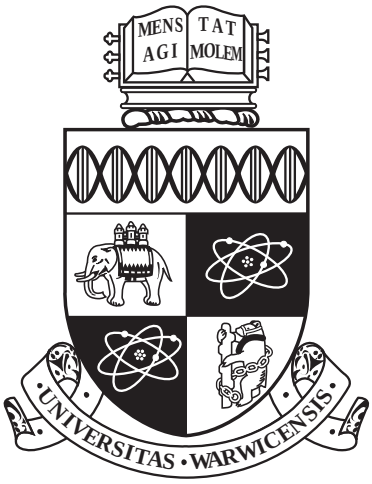

Ring Polymers as Topological Glass, a New Phase of Matter?

by

Wei-Chang Lo

Thesis

Submitted to the University of Warwick

for the degree of

Doctor of Philosophy

Department of Physics

December 2011

THE UNIVERSITY OF
WARWICK

Contents

Acknowledgments

In the past three years, many have assisted and supported me to complete this thesis. First of all I want to express my greatest gratitude to my supervisor, Professor Matthew Turner, for his enlightening supervision over my Ph.D. research and the introduction to the British culture. I also greatly appreciate his supportive role as my supervisor to help me solve many difficulties outside of the research.

I am sincerely grateful to Professor Andrew Turberfield and Dr. Jonathan Bath for their roles of the research collaboration. Professor Turberfield has always been supportive to this experiment project and granted me to access the research facilities of his group. Dr. Bath's expertise in molecular biology has helped me since the very beginning of the project. Without him I could not have completed the experiment on time. Thanks to Dr. Sonia Antoranz Contera for her kindly offering laboratory equipments. I also want to thank Dr. Helen Carstairs, Dr. Carlos Sanchez-Cano, Adam Wollman, Robert Machinek, Dr. Richard Muscat, Katherine Dunn, Dr. Mireya McKee and Sarah Matthews, for their kind assistance to my experiment and the lovely lunch conversation.

I have my special thanks to Professor George Rowlands, Professor Robin Ball and Dr. Davide Marenduzzo, for the helpful discussion of the theoretical models and simulations, also for the delightful and joyful conversation about physics and history with Professor Rowlands during the department coffee/tea time.

The full sponsorship from the Department of Physics, University of Warwick, is greatly appreciated. In particular, I want to thank Professor Geetha Balakrishnan for her role as the postgraduate tutor at the time when I applied for the Ph.D. position in 2008. I also want to thank the group members, Jamie Luo, Matthew

Thomas and Dr. Chris Brackley, for all the academic discussions of physics and sciences in general and the entertaining conversation in the past three years.

Last but not least, I want to thank my parents, sister, brother and sister-in-law for their long standing support back in Taiwan. I also have special thanks to my girlfriend Chia-Yu, for her always being supportive and encouraging me when I lost faith to pursue the academic career of sciences.

Abstract

In this thesis the dynamic properties of unknotted ring polymers at high densities is investigated. We hypothesise an unusual type of glass transition which is purely attributed to the topological constraints between the penetrating rings.

A mean-field model is developed to describe the strongly constrained ring polymers as ideal lattice trees. Equilibrium properties can be derived within the framework of statistical thermodynamics using an argument based on structural recurrence. Here each ring can be seen as a linear object—as a loop strand with branching protrusions.

The ring polymers were simplified as loop strands without any branching. We focused on the constraints emerging from the circular topology, and the polymer dynamics was simulated using a Monte Carlo technique. The degree of inter-ring penetrations essentially controls the slowing of dynamics and represents a universal parameter for the glass transition. The penetrating rings form a percolating network involving reversible quasi-topological entanglements. As such, the stress relaxation of each ring is prolonged by the coupled penetrations which have limited pathways to release constraints from one another.

The simulation data suggest the existence of a glassy material exclusively formed by the topological constraints associated with the circular structure. In order to test the picture of topological glass, the fluorescence-labelled circular DNA was used to observe its self-diffusion in the entangled state. The experimental method has demonstrated its potential for the future investigation of the dynamics of entangled ring polymers despite the fact that it failed to provide evidence of the glassy state in our experiment.

Chapter 1

Introduction

Amorphous solids are found all around us. These materials lack the long-range order characteristic of crystalline solids and exhibit a broad range of diverse physical properties; an amorphous solid can be as soft as a polymer gel or it can be as rigid as obsidian. Among the amorphous solids, glass is the oldest one utilised by human and of the widest applications in our daily lives. It is usually formed by cooling a viscous liquid rapidly, like the lava in the case of obsidian. The process of viscous liquids becoming rigid, brittle disordered solids is called the glass transition.

While a great deal of work continues to be published on the glass transition in various physical systems, including colloids [Dyre, 2006; Binder and Kob, 2011; Berthier and Biroli, 2011] and polymers [Turner, 1978; Schweizer, 1989a; Angell, 1995], a complete understanding of this transition remains elusive. The glass transition has several characteristic properties including a dramatic (usually exponential) slowing of dynamics for temperatures above a glass transition temperature T_g (which is itself often not well defined) combined with the lack of any crystalline order. Beyond these general features the glass transition appears to lack universality—its properties vary according to the microscopic details of the particular system.

The fundamental mechanism involved in the glass transition is not well understood albeit the long history of manufacturing glass since the ancient Egypt, but it is interpreted as a direct result of the frozen molecular motion. Among the glass formers, polymers are of particular interest because of their wide applications. The frozen molecular motion below T_g in polymers is largely contributed by the topological constraints due to their repetitive structures distinct from that of the simple, low molecular weight glass formers. Since there are multiple ways to modify the structure of a polymer to change its T_g, being inserting stiff monomers or adding pendant groups, we are thus inspired to hypothesise an unusual form of glass

transition only can be found in polymers of the circular topology.

In the present thesis we study high molecular weight ring polymers at high densities. We are interested in melt of the ring polymers or their concentrated solutions in good solvents where the topological constraints have strong effects on both their static and dynamic properties. We assume that the ring polymers are synthesised as trivial rings and remain unknotted, in the strict topological sense, throughout the polymerisation process. There is now a significant body of literature on ring polymers, including on their static properties [Cates and Deutsch, 1986; Müller et al., 1996; Brown and Szamel, 1998; Suzuki et al., 2008; Vettorel et al., 2009] with continuing contemporary interest in their conformations in the entangled state [Suzuki et al., 2009; Halverson et al., 2011; Rosa et al., 2011]. Experimental progress has been made on the synthesis of ring polymers with few knots and concatenations but experiments are still difficult, due to contamination by linear chains, polydispersity and the inherent limitations of rheological measurements. In particular it is challenging to measure the rheology associated with the extreme (long lived) tail of stress relaxation, and the rheological properties are known to be sensitive to contamination from linear polymers [Roovers, 1988; Robertson and Smith, 2007; Kapnistos et al., 2008].

Despite years of effort investigating ring polymers, we believe there is at least one interesting aspect that has been overlooked by these previous studies. It is usually assumed that the ring polymers collapse and segregate when they are brought into close contact. However, some recent computer simulations [Halverson et al., 2011; Rosa et al., 2011] showed that the structure of these rings were not as trivial as many had expected; the entangled ring polymers segregated in the sense of scaling law, but part of each ring polymers also protruded and entangled with other polymers. We speculate the unknotted and unconcatenated rings could also penetrate each other without violating the topological constraints. This can be achieved by extending an arm of loop from one ring polymer and threading this arm through the middle of another ring polymer.

The penetration surely would influence the dynamics of ring polymers because their motion would be farther restricted. With a high frequency of penetration between the ring polymers, the molecular motion can be strongly hindered by the non-crossing constraint. As a result, the stress relaxation of these rings can be significantly slower and make it resemble a glassy material. Since the slowing of stress relaxation is exclusively attributed to the unique topology of ring polymers, it is called the topological glass to be distinguished from the common glass. As yet there is no evidence for the kind of transition that we predict in this thesis but we believe

that this does not preclude its existence due to the experimental limitations noted above.

In this thesis the detailed investigation of entangled ring polymers is presented. Our research has been conducted through various approaches utilising theoretical models, a Monte Carlo simulation and an experiment using fluorescence microscopy. The content of the thesis is organised as follows. In Chapter 2 we will briefly review the preceding studies of ring polymers. It will be mainly focused on the properties of ring polymers in melt or in gels. Chapter 3 is dedicated to a mean-field model based on the concept of lattice trees. This model will be analysed within the framework of statistical thermodynamics with the argument of structural recurrence in the lattice tree. The analysis offers insights of the equilibrium properties of entangled ring polymers and the clues of calculating the dynamics of such polymers. In Chapter 4 we will exploit the results shown in Chapter 3 to construct a coarse-grained model, which was employed in the Monte Carlo simulation. The simulation data indeed demonstrate that the topological constraints contributed by the penetration of rings significantly extend the process of stress relaxation. We consider that the simulation data reinforce our picture of how these polymers might form the topological glass. In Chapter 5 we present a discussion of our fluorescence microscopy experiment performed on concentrated DNA solutions. A more detailed discussion of the results of Chapter 3–5 is given in Chapter 6. The implication of these results regarding the existence of the topological glass is examined as well. At the end, the conclusions of this study will be drawn in Chapter 7.

Chapter 2

From Entangled Ring Polymers to Lattice Trees

Polymers are constituted of single or multiple linear chains, which are composed of repeating units joined via covalent bonds. For example, star polymers are made of several linear chains attached to a multifunctional group at the centre, forming a starfish-like structure. The ends of these linear chains play an important role in many properties of polymers, such as the reptation mechanism in melt and gels [de Gennes, 1971]. However, ring polymers represent a peculiar class among polymers since they have no chain end [McLeish, 2002a], thus one may expect that many properties of ring polymers must be different from those of other classes. Although ring polymers are not as common as linear polymers, effective protocols to synthesise ring polymers have been found since the 1980s. Besides synthesised ones, there are naturally occurring ring polymers like plasmid DNA, the circular extrachromosomal DNA present in many bacteria. Despite extensive studies on plasmids due to their potential applications in genetic engineering, there is continuing interest in examining the physical properties of plasmids, for instance, the branching structure and elasticity of supercoiled DNA [Marko and Siggia, 1995b; Marko, 2007; Forth et al., 2008; Clauvelin et al., 2009]. Through these studies one may gain a more thorough understanding of these materials and help future innovations and technological progress in diverse fields.

2.1 Static Conformations of Ring Polymers

2.1.1 Topological Constraints of Entangled Ring Polymers

Ring polymers have puzzled many scientists and engineers for years. For a single ring polymer in a good solvent, i.e. the dilute limit, one may imagine its static and dynamic properties are quite easy to understand. Unfortunately the situation is not as simple as it appears. For example, Zimm and Stockmayer [1949] and Klein [1986] had analysed how such a ring polymer would behave in a solvent. In certain situations, such as with Θ conditions so that the polymer had no excluded volume interaction, the calculation was straightforward. However, the unique topology of ring polymers introduces constraints that are very distinct from other polymer classes, particularly when one acknowledges the probability of forming knots or concatenations during polymerisation. In fact, de Gennes [1979] had imagined a fascinating kind of polymer gels based on the topological constraints. Without bonding to form crosslinks, what he called an *Olympic gel* was formed by concatenated ring polymers, which would look like medieval chain mail armour.

If the rings are unknotted and unconcatenated, they impose the topological constraints on themselves and on each other when they come into close contact. Des Cloizeaux argued that, for long flexible rings in solutions, the topological constraints and the excluded volume interactions would have similar effects [des Cloizeaux, 1981]. He pointed out that the knotted configurations had to be excluded in order to maintain the ring as a circle. The calculation was proceeded by using the Gaussian invariant to find the linking number of two rings. This approach could not always specify the configurations between these two rings, an obtained linking number might refer to either the two rings were linked or not. Under such circumstances, carrying out the calculation required further approximate assumptions.

The difficulty of analysing ring polymers is more visible if one compares the topological constraints of ring polymers with that of linear polymers. For linear polymers the non-crossing constraints have great effects on their dynamic properties but not on the static properties, since all configurations are still accessible. Many important breakthroughs have been done by developing mean-field models like the tube model to depict the dynamics of entangled linear polymers. In the tube model, for example, the non-crossing constraints posed on a polymer are viewed as if there is a *tube* surrounding it [de Gennes, 1979; Doi and Edwards, 1986].

However, the topological constraints also strongly affect the static properties of entangled ring polymers. In order to calculate the equilibrium properties, one needs to consider all the possible configurations and exclude those violating

the topological constraints, for instance, the concatenated or knotted rings. To rigorously express such a system in a mathematical model is extremely difficult. As mentioned above, the Gaussian invariant can be used to distinguish whether polymers cross each other, it is not enough to specify the topological class of ring polymers in contact [Doi and Edwards, 1986, pp. 156–159]. For instance, a pair of separated ring polymers is not distinguishable from certain ways in which they are knotted.

Arguably the complicated mathematics related to the topological constraints is one of the reasons why the theories describing ring polymers are not as well established as for other polymer architectures. Many have recognised these issues and tried to build an analogue of the tube model for entangled ring polymers. Although a ring polymer has no end to explore new paths and to *disengage* itself, the entanglements formed by neighbouring chains act as a barrier to confine its motion in a manner that is similar to that in entangled linear polymers. Therefore, a great deal of work since the 1980s has been based on the concept of *lattice animals*[1], which is covered below.

2.1.2 Statistical Sizes of Entangled Ring Polymers

Because of the great success of the tube model, many researchers attempted to describe entangled ring polymers in a similar way. To avoid the complication of certain configurations, which will be covered later in this thesis, a well defined system for the current discussion is a ring pulled in between an array of fixed obstacles. This corresponds to the case of a ring in gels without concatenation, and it has been considered as a preliminary model of entangled ring polymers. Since the ring is unable to cross the obstacles, many have conjectured that the ring must adopt the conformation of a lattice tree to accommodate itself within the array of obstacles.

In their seminal paper, Cates and Deutsch [1986] analysed the statistics of ring polymers in gels and melt and their dynamic properties with the topological constraints and the excluded volume interactions by following the concept of lattice trees. The radius of a ring polymer in gels was thought to follow the same scaling law as a branched polymer with excluded volume interactions. This led to the result that the radius followed a Gaussian distribution [Parisi and Sourlas, 1981]. They further argued that ring polymers in melt were unlikely to follow the same Gaussian distribution as a ring would be in gels. They applied a Flory-like scaling analysis

[1] In this thesis we will use the term *lattice tree* rather than *lattice animal*. The main difference between them is that closed loops are allowed in a lattice animal. This of course does not make sense at all for ring polymers since any arbitrary linear section of the lattice tree or animal actually represents a duplex structure of the constrained ring polymer.

to this system which yielded the prediction as follows. The radius of rings R scales with the degree of polymerisation N as $R \propto N^{2/(\delta+2)}$, where δ is the dimensionality of space, or simply $R \propto N^{2/5}$ in three dimensions.

This result has been supported by some later computer simulations. For example, Müller et al. [1996] used the bond fluctuation model, a dynamic Monte Carlo method, to simulate such systems. They obtained an exponent $\nu \approx 0.39 \pm 0.03$ for the average ring radius $R \propto N^{\nu}$, and the result is in agreement with Cates and Deutsch's prediction. Brown and Szamel [1998] also obtained a similar result by employing the bond fluctuation model, and the result gives $\nu = 0.42$ for the radius of gyration $R_g \propto N^{\nu}$. In a later paper, Brown et al. [2001] again obtained a similar result $\nu = 0.415$.

However, these computer simulations suffered from unavoidable limitations on polymer contour length L and the total number of polymer chains N_c due to the limitation of computation hardware at the time. Further hindering simulations was the fact that the entanglement length l_e (the average contour length of chain between effective entanglements) can be $\sim 10^2$ monomeric units [Kremer and Grest, 1990; Vettorel et al., 2009]. Universal results of the scaling law will only be found for long enough polymers, i.e. those with a large number of entanglements. Computer simulations that explicitly include monomeric units are therefore effectively handicapped by two orders of magnitude in system size. These simulations did not properly explore the entangled regime, and the results were likely to be in the crossover region.

Indeed several more recent simulations showed different scaling laws from the prediction $\nu = 2/5$. These results suggest that the $\nu = 2/5$ behaviour is only a crossover to the collapsed rings ($\nu = 1/3$). For instance, Suzuki et al. [2008] found that the exponent ν decreased with increasing N. The authors concluded that ν was in the range of $1/3 \leq \nu \ll 0.365$ when the molecular weight of a ring polymer was high enough. Vettorel et al. [2009] carried out a Monte Carlo simulation on a simple cubic lattice. They found the sufficiently long rings behaved as compact objects and their radius scaled as $N^{1/3}$ for large chain length N. Even in a following paper of their original simulation, Müller et al. [2000] discovered the same result. They tuned the persistence length to increase the ring overlap required for the mean-field picture to hold. As a result, the new simulation then demonstrated that the exponent decreases down to $\nu \lesssim 1/3$ with increasing persistence length.

Although there have been many theoretical and numerical analyses of entangled ring polymers, experimental evidence of the static properties is scarce. There were a few reported experiments which probed the radius of gyration of ring poly-

mers in melt by scattering experiments. Arrighi et al. [2004] investigated ν for ring polymers in melt using neutron scattering, and they found $\nu = 0.42$. The molecular weight of the samples used in this experiment was less than 15,000. Takano [2007] also performed a neutron scattering experiment and obtained $\nu = 0.34$. Notably the author specified that the percentage of linear contamination of the sample was 4% or less.

2.1.3 Penetrations between Ring Polymers

As explained above, few formal theoretical results exist for ring polymers due to the difficulty in handling the essential non-locality of the topological constraints. The problem would be much more tractable were chains able to pass through one another like so-called phantom chains. Instead the assumption that they cannot do so at once makes the problem difficult but also results in their unusual physics of interest to us. Most of the existing theoretical studies adopt the approach of representing a constrained ring polymer as a lattice tree. To make the model consistent with the original system, the excluded volume interactions are included such that the trees become self-avoiding. This prevents the rings from penetrating each other.

Currently the consensus regarding the scaling of the radius of entangled ring polymers seems to favour $R \propto N^{1/3}$ for the high N limit, and the scaling suggests that the ring polymers tend to collapse and segregate at a high density. The segregated ring is seen by many as a self-consistent interpretation of the dynamic behaviour measured in the experiments. These measurements showed that the ring polymers were less entangled and exhibited faster relaxation than their linear counterparts. Nevertheless, some recent numerical studies have raised the question upon the picture of the fully segregated ring polymers.

Suzuki et al. [2009] employed Monte Carlo simulations using the bond fluctuation model and calculated the segment density $\rho(r)$ of each ring polymer in melt, where r is the radial distance from the centre of mass of a ring polymer. The segment density decreased with the increasing distance r. For an ideal chain $\rho(r)$ should have decreased continuously with increasing N. Contrary to that, they found $\rho(r)$ was bound to a value with sufficiently large N. They concluded that, although the ring polymer would tend to squeeze itself rather to penetrate into the neighbouring molecules, it was not completely segregated from the surroundings.

Furthermore, Bohn and Heermann [2010] investigated the interactions between two ring polymers, and they found that the rings were strongly elongated and aligned perpendicular at short separations. Halverson et al. [2011] conducted molecular dynamics simulations to investigate the structural properties of uncon-

catenated ring polymers in melt. Despite they reproduced the result of $\nu = 2/5$ crossing over to $\nu = 1/3$ for the long chain limit, the further analysis showed these rings were very irregularly and self-similar shaped objects. As a result, they suggested the rings in the melt, although reasonably segregated in the scaling sense, had significant protrusions into one another.

Intuitively these protrusions or penetrations should result in a different dynamic behaviour from that of the self-avoiding lattice trees, especially when their number per ring polymer exceeds a threshold value. One may appreciate why this is the case by taking a box of entangled rubber bands as a conceptual example. When the density of rubber bands is high enough and they have been stirred for a long time, there are a lot of rubber bands penetrating surrounding ones and sometimes themselves, simultaneously. If one slowly extracts a rubber band from the box, a number of the rubber bands will move together, as if the whole is a single solid body. This sort of behaviour cannot be modelled within the framework of the self-avoiding lattice tree.

2.2 Dynamics of Entangled Ring Polymers

2.2.1 Theoretical Models of the Dynamics

In Section 2.1 we reviewed the preceding investigations of the static properties of entangled ring polymers. We surmised that the entangled ring polymers might not simply collapse and segregate. As a result, the dynamics of these entangled ring polymers should reflect this due to the topological constraints affecting both the static and dynamic properties. In any case, however, derived results can be very different from one another, depending on which model is applied to studying this system.

Without any surprise, there are even fewer theoretical studies of the dynamic behaviour of entangled ring polymers in the literature. We already explained in Section 2.1 that a first-principle theory for the entangled ring polymers is very difficult. It is usually assumed that the microscopic process of relaxation in entangled ring polymers is in the same manner as that in entangled linear polymers. Then the calculation is performed using simple models like the lattice tree. For example, a ring polymer in a gel can be modelled as a self-avoiding lattice tree.

The diffusion constant of the centre of mass of such a ring polymer can be easily estimated if we adapt de Gennes' picture of *kink gas*, i.e. the non-interacting length defects, to the ring polymer [de Gennes, 1971]. The self-diffusion of the whole ring polymer essentially is proceeded by the transport of length defects along the

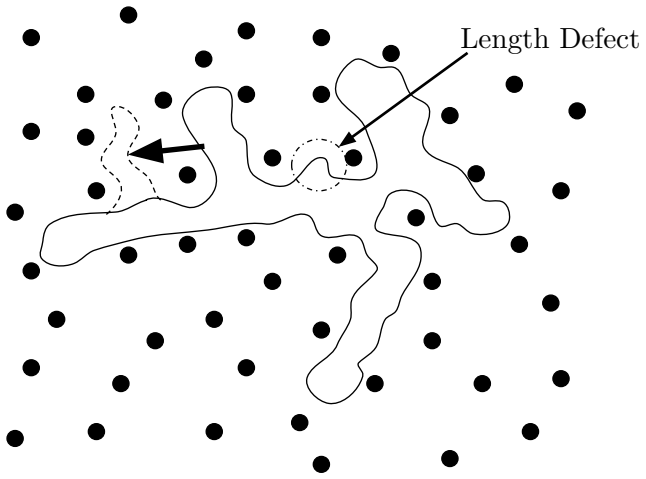

Figure 2.1: A ring polymer confined between fixed obstacles (closed circles). The translational displacement of the whole ring is proceeded by the diffusion of length defects. Accumulating the random migration of length defects all around the contour, a whole arm of loop can move around the obstacles, as indicated by the bold arrow and the dashed line.

chain contour [Cates and Deutsch, 1986; Rubinstein, 1986]. These length defects are supposed to diffuse in the same way as those on a linear chain. The time required for a length defect to diffuse along the contour for a distance equivalent to the radius of the ring R can be estimated according to the scaling of R mentioned in Section 2.1. The number of length defects scales with N since there is no end to relax these length defects. Combining these results, it is straightforward to obtain the translational diffusion constant of the ring polymer. Both groups of authors derived $D \propto N^{-2}$ and the relaxation time $\tau \propto N^3$.

However, Obukhov et al. [1994] argued that, also considering a ring polymer in a gel, the diffusion of length defects along the polymer contour differed from that on a linear chain. The ring polymer was also modelled as a lattice tree, formed by a trunk and branches. There should be two different processes involved. The first step is the migration of length defects within the branches, and the second one involving the diffusion of length defects along the trunk. They suggested that these previous work had overlooked some modes of motion available to a ring polymer thus the rate of evolution of polymer configuration was underestimated. They obtained the same result of diffusion constant $D \propto N^{-2}$ but a different scaling of the relaxation time, $\tau \propto N^{5/2}$. Taking a different approach, Iyer et al. [2006] adopted a dynamic model inspired by the pom-pom model of branched polymers and also obtained results which agreed with those of Obukhov et al. [1994].

2.2.2 Viscoelasticity and Rheological Measurements

Experimentally a common strategy to study the dynamics of non-Newtonian fluids, such as concentrated polymer solutions, is to perform rheometry. By measuring responses of bulk material against a small deformation, one is able to extract information of the dynamics of the material. In the case of polymers, particularly when they are entangled, the topological constraints contribute to the viscoelasticity. The viscoelastic properties, such as the zero-shear viscosity and the relaxation modulus, are widely used to characterise polymers and to probe their microscopic structure at a certain level of length scale and above. Meanwhile, rheometry is also very useful to identify characteristic time scales of relaxation in these non-Newtonian fluids.

Roovers had measured the rheological response of synthesised ring polymers of polystyrene and polybutadiene [Roovers, 1985, 1988]. It was observed that the melt viscosity of the ring polymer tested was about 10 times smaller than that of the linear polymers with the same molecular weight. McKeena et al. [1989] used the measurement of recoverable compliance to address the question of the fraction quality in the ring polymer prepared by several groups [McKenna et al., 1987; Roovers, 1985]. Orrah et al. [1988] measured the low-shear bulk viscosity of cyclic and linear poly(dimethylsiloxane) (PDMS). The critical molecular weight for entanglement (M_c) of these samples was estimated. They found that both cyclic and linear PDMS had the same M_c and the same scaling of the viscosity $\eta \propto M^{3.4}$, where M is the molecular weight.

Unfortunately these data are not enough to be compared with the theoretical analyses in a systematic way. These experiments did not necessarily explore the same regime as the chemical structure and concentration of the samples varied from one to another. The results are not always consistent with each other either, thus it is difficult to conclude any universal property from them. For entangled polymers, the data of rheological measurements are only applicable to detecting structures which have a length scale above the entanglement length. It is questionable whether or not these data genuinely represent the microscopic structure of the entangled ring polymers. There could be several factors affecting the outcome of the rheological measurements, such as polydispersity, linear contaminants and so on.

Notably the question of within which range of concentrations (or molecular weights) the lattice tree picture is valid will be the key of using the experimental data. One expect that the model is valid when each ring polymer is sufficiently entangled. It is obvious that the concentration must exceed the overlap concentration $C^\star$, the concentration at which the coil volume of a polymer starts to overlap with that of the neighbouring polymers. However, beyond $C^\star$ it is unclear at which

concentration the picture of lattice trees starts to be a good representation of the entangled ring polymers. Moreover, the theoretical analyses usually did not offer accessible predictions to rheological measurements, like the plateau modulus or the complex modulus. The lack of theoretical predictions on these quantities makes the comparison between models and experimental data very difficult.

2.2.3 The Problem of Contamination in Ring Polymers

One of the factors which potentially affect the experiment is the issue of polydispersity. More specifically, it is not just of ring polymers in different sizes but also of the contamination of linear polymers among the rings. There is evidence which shows that contamination of linear chains, even in trace amounts, can greatly affect the viscoelasticity of ring polymers. This is not surprising at all since it has been proved that rheological measurements are particularly sensitive to changes in molecular topology on the scale of entanglement length and above [McLeish, 2002b]. Roovers [1988] concluded that rings contaminated with 20–25% linear polymers had the same melt viscosity as linear polymers, although the plateau modulus was only about half of that of linear polymers. Using the method of *liquid chromatography at the critical condition*, Kapnistos et al. [2008] obtained properly purified ring polymers and measured the relaxation moduli. They also used purposely contaminated samples to show that even 0.1% linear contaminants was sufficient to change the measured relaxation modulus. By using their data as basis of calibration, they concluded that many previously reported data had possibly been affected by a trace of linear chains.

Other than synthesised ring polymers, circular DNA also has been used to study properties of entangled ring polymers and, in particular, the differences of dynamics between blends of ring and linear polymers [Robertson and Smith, 2007]. In their measurements with 45 kilo base pairs (kbp) DNA at 1 mg/mL, the circles diffused about 100 times slower when surrounded by linear molecules than when surrounded by circles. Linear DNA diffused about 10 times slower when surrounded by its own kind than the circular DNA surrounded by circles. More importantly, the diffusion constant of linear DNA surrounded by circular ones is only about 80% of the circular DNA surrounded by its own kind. This experiment demonstrated that the diffusion of DNA strongly depended on topology of both the marked molecules and the surrounding molecules.

From these researchers' efforts we may summarise that the difficulties of studying ring polymers arise from their unique closed structure and the challenge of purification. The non-local topological constraints are difficult to handle mathe-

matically. In some experiments like rheological measurements, trace contaminants in ring polymers can affect the obtained results drastically. Such contaminants like unclosed linear chains or knotted ring polymers are common products of most polymerisation processes. Without an effective purification method, the results of experiments will be difficult to interpret, as Kapnistos et al. [2008] concluded.

2.3 Conjectures on Topological Glass

2.3.1 Polymer Glass and Glass Transition

It has been emphasised in the last two sections that the topological constraints of ring polymers significantly affect both their static and dynamic properties in melt. We also introduced the idea of penetrating rings which could cause different behaviour of the rings in such melt. This picture leads to the main topic of this thesis, the topological constraints affect the molecular motion and make the ring polymers resemble a glassy material.

The glass transition of polymers is of great interest in industry. Many commercial products of polymers are actually used in the glassy state, for example, thermoplastics such as polystyrene and poly(methyl methacrylate). Despite its great importance in a lot of daily applications, a detailed theoretical description of the glass transition in polymers is lacking. Generally speaking, the topological constraints of entangled polymers make them good glass formers since the molecular motion can be greatly prohibited, but the mathematics of describing the transition process is inevitably complicated. Currently the most successful theory for quantitative calculation of the dynamics of glass-forming is the mode-coupling theory [Binder and Kob, 2011]. However, the classic mode-coupling theory is only useful for simple or low molecular weight liquids, such as silicates or propylene carbonate. Nonetheless, some researchers have tried building an extended mode-coupling theory for the polymer glass transition [Schweizer, 1989a,b; Chong and Fuchs, 2002].

There are many routes to form glass, but the normal mode of glass formation is cooling of a viscous liquid [Angell, 1995]. It has been observed that the viscosity (η) of glass formers strongly increases when the temperature is decreased within a certain range. This range of temperature depends on the chemical compositions of the liquid, therefore a temperature called the *glass transition temperature* T_g is usually defined by means of $\eta(T_g) = 10^{12}$ Pa·s to characterise the point where the liquid becomes glass [Binder and Kob, 2011]. The detailed processes involved in the glass transition are not yet fully understood, as there are many liquids with different properties which are found to be glass formers. For example, silica and polystyrene

have absolutely different molecular structures but they all can form glass, even though silica has a much higher T_g (fused silica $\approx$1200°C) than polystyrene (95°C).

Nevertheless, it is thought that the processes of glass transition are related to the hindrance of molecular motion. The molecules in a glass former are either forced to move in a cooperative way [Adam and Gibbs, 1965] or only have very limited free volume to move (the so-called *cage effect*) [Cohen and Turnbull, 1959]. In any case, the relaxation time of these molecules becomes very long, which is reflected in the strongly increased viscosity near T_g. For polymer melt it is natural to form glass without difficulties. First of all it is difficult for entangled polymers to align in crystalline orders, although sometimes a bulk of polymer is partially disordered and crystalline simultaneously. Secondly the entanglements between polymer chains become effective barriers against the relaxation of polymer chains. This of course leads to the well-known results given by the reptation and the tube model. However, making the entangled polymers become glass will require further constraints to suppress the relaxation modes, such as the reptation and the contour length fluctuation. A full microscopic theory to explain the polymer glass transition is beyond the scope of this thesis. The special topological constraints that only can be found in ring polymers, on the other hand, is what motivates this research.

2.3.2 Topological Glass

The topological constraints as well as the non-crossing constraints of polymer chains play an important role in the glass transition of polymers. It is known that the introduction of relatively stiff chemical groups (such as benzene rings) or pendant groups can interfere the motion of polymer chains and hence increase T_g [Cowie and Arrighi, 2008]. In this thesis we consider a hypothetical type of polymer glass which is caused by the unique topology of ring polymers. As we have already illustrated in the conceptual example of rubber bands, the penetration between rings may greatly change the dynamics of entangled ring polymers. The relaxation of each ring polymer now is not just restricted by the surrounding polymers, the temporary blockage of the penetrating rings will further restrict the available relaxation modes.

If the number of penetrations per ring polymer exceeds a certain level, which is likely related to the concentration of the ring polymers, a large number of the ring polymers can form a giant cluster via the penetrations. When the system reaches such a state, the relation of penetrations between rings can be treated as a problem of percolation. For these rings in order to escape from the trapped state, the penetrations can only be removed through a limited set of routes. As a result, the relaxation time of each ring polymer will be extremely long, and, once it is much

longer than the time scale in experiments, the ring polymers can be seen as in a glassy state.

To our knowledge so far, there is no research dedicated to this kind of glass formers. For one thing a theoretical analysis for entangled ring polymers is a difficult task, for the other to produce highly purified ring polymer samples is a demanding job. The only related research we have found in the literature is possibly the glass transition of DNA [Norberg and Nilson, 1996; Sokolov et al., 1999; Grunina et al., 2006]. This is of great interest in biology since the glassy form of biopolymers is used to preserve biological functions in some species when facing harsh environments [Angell, 1995]. Disappointingly, though, we do not find any specific study of glass transition in circular DNA.

In this thesis we are going to demonstrate our study of the dynamics of entangled ring polymers. In spite of our interest in the glass transition of ring polymers, it is not our intention to study this system near its T_g. On the contrary, it is the state where these rings are still able to penetrate and disengage, namely the equilibrium ($T \gg T_g$), that attracts our attention. We expect that, even at a temperature far above T_g, such a system can show significantly slower relaxation time simply due to the topological constraints. Furthermore, even the system is far from the glass transition, it exhibits some similar behaviours as those glass formers near their T_g.

Chapter 3

Statistical Properties of Constrained Lattice Trees

In this chapter we will proceed to discuss the mean-field description for entangled ring polymers. In such environments the ring polymers suffer from the topological constraints from themselves and other neighbouring ones, thus we postulate that they are forced to adopt conformations resembling lattice trees [Cates and Deutsch, 1986; McLeish, 2002a]. We will explore this concept within the framework of statistical thermodynamics and incorporate the idea of penetrating rings into the model of lattice trees.

3.1 Historical Background

As we have mentioned in Chapter 2, the conformation of an unknotted ring polymer in an array of fixed obstacles is thought to resemble lattice trees. This is reasonable since the conformation is restricted due to the non-crossing constraints posed by the obstacles. Likewise, many have conjectured that the conformation of entangled ring polymers, e.g. in melt, should show a similar structure. Also there is numerical and experimental evidence indicating that the scaling exponent of the radius of entangled ring polymers falls between a Gaussian chain ($\nu = 1/2$) and a collapsed one ($\nu = 1/3$). These results demonstrate similar exponents to those of branched polymers, and it seems sensible to approximate the conformation of entangled ring polymers as lattice trees. However, there is to date no validation of this approximation, thus it is difficult to assess its range of validity.

One advantage of modelling entangled ring polymers as lattice trees is that the lattice tree shares many similar characteristics with branched polymers. It is

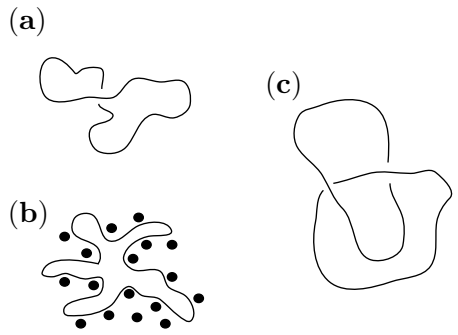

Figure 3.1: A schematic diagram showing the topological constraints of ring polymers under various circumstances. (**a**) A ring polymer in solutions which looks like a random coil. (**b**) A ring confined by fixed obstacles. It is forced to adopt such a conformation due to the non-crossing constraints. (**c**) Two concatenated rings. This is forbidden in our calculation, because the rings do not enclose any other chains throughout the polymerisation process.

not difficult to see why by comparing their conformations. Both branched polymers and lattice trees are constructed by linear sections attached to each other at certain points. The biggest difference, though, is that in branched polymers these branching points are formed by multifunctional groups via covalent bonds. Once the polymerisation process is terminated, the branching structure will not change thereafter. For lattice trees it is not necessarily the case[1].

Branched polymers have been extensively studied since the 1940s [Flory, 1941a,b,c; Stockmayer, 1943, 1944] because of their role in the gel formation, in which branched polymers build up an infinitely large network structure with crosslinks. However, most of the theoretical analyses of branched polymers in melt were conducted much later after the concept of reptation and the tube model had been established. In the following text of this section, the relevant properties of branched polymers to our problem of ring polymers will be introduced.

As mentioned in Chapter 2, a ring polymer in an array of fixed obstacles can be properly modelled by a lattice tree. Its static properties, such as the radius of gyration, should be equivalent to that of a randomly generated branched polymer. Such static properties have been investigated via direct calculations [Zimm and

[1]This is probably the reason why many used the term lattice animals rather than lattice trees, regardless of forming a loop in the structure. It seems natural to call the constrained ring polymer an animal since the branching points are not fixed so that it can alter the shape like an amoeba.

Stockmayer, 1949], on the Bethe lattice (namely the Cayley tree) [Khokhlov and Nechaev, 1985], by field theories [Lubensky and Isaacson, 1978, 1979], the Lee-Yang edge singularity [Parisi and Sourlas, 1981] and the method of dimensional reduction [Imbrie, 2003]. It was found that the radius of gyration of an ideal branched polymer followed the relation $R_g \propto N^{1/4}$ [Zimm and Stockmayer, 1949]. On the other hand, the radius of gyration was found to follow a Gaussian distribution as $R_g \propto N^{1/2}$ when the excluded volume interactions was included [Parisi and Sourlas, 1981]. This result coincidentally is the same as that of ideal random walks.

Furthermore, there exists another system which behaves similarly to our picture of constrained ring polymers in melt. In many aqueous surfactant solutions, amphiphiles are found to assemble reversibly into various structures, depending on the conditions such as the shape of amphiphiles, the concentration and so on. There is a certain type of structure called a wormlike micelle, which is a long, flexible branched object. Since its branching is randomly formed by the aggregated amphiphiles, the branches can be spontaneously manipulated or even eliminated. Once these wormlike micelles reach a high density, they can form entangled viscoelastic fluid. The dynamics of these entangled wormlike micelles can be accounted by the extended reptation model [Cates, 1987], although sometimes extremely long wormlike micelles exhibit higher fluidity than expected [Lequeux, 1992].

From our point of view, however, none of the models mentioned above are satisfactory to describe the dynamics of entangled ring polymers. In the case of wormlike micelles, the branched structure can be broken and altered by moving away a column of the surfactants, or it can attach to others. This is not the case for entangled ring polymers, as the diffusion of kinks along their contours is the only mechanism for transferring material, and this should change the whole conformation in a continuous manner. More importantly, for both the self-avoiding lattice tree and the wormlike micelles, the models do not account for the situations in which the rings penetrate each other. The excluded volume interactions of the self-avoiding lattice tree repels any segment closer than a correlation length. Clearly no primitive path of any linear section is able to penetrate any other. Although wormlike micelles are able to connect to one another, the process and the constraints involved are very different from that of entangled ring polymers.

When the density or the molecular weight of ring polymers reaches a threshold, we expect that a significant portion of the rings will penetrate other rings. This forms extra quasi-topological entanglements that prevent the rings moving freely, as the conceptual example of rubber bands in Section 2.1. Therefore we anticipate a much slower stress relaxation may occur in such systems. Still, in order to in-

vestigate the dynamics of entangled ring polymers analytically, a simple model is necessary to begin with. In this chapter a modified model of lattice trees is applied to studying the equilibrium of entangled ring polymers. The lattice tree will be deconstructed into multiple parts, and the corresponding grand canonical partition functions will be derived to calculate statistical properties.

3.2 Constrained Lattice Trees

3.2.1 Phantom Chains

We consider the case of a compact unknotted ring polymer in melt of its own kind and neglect the excluded volume interactions. In the concentrated regime we adopt the ansatz in which each ring takes the configurations resembling lattice trees as explained in Section 2.1 and 3.1. Each segment of the lattice tree is made up of duplex pairs of polymer chains, one outward and the other returning within the volume of a segment. In this thesis the lattice tree is assumed to be made up of N_s segments, each of which has a physical length l_s, with a coordination number z.

Consider that such a lattice tree has u branches extruding from a linear backbone, formed by N_l segments; see Figure 3.2. Let N_r represents the set of these numbers of segments, $N_r \equiv \{N_1, N_2, \cdots, N_u, N_l\}$, in which the elements satisfy

$$N_l + \sum_{i=1}^{u} N_i = N_s. \tag{3.1}$$

Suppose that the backbone has an end-to-end distance r, the partition function of the whole lattice tree can be expressed by

$$Z(r) = \sum_{N_r} Q_s(N_r) Q'_{N_l}(r) \prod_{i=1}^{u} Q_{N_i}. \tag{3.2}$$

Q_{N_i} and Q'_{N_l} are the canonical partition functions of the extruding branches and the linear backbone with the given number of segments, respectively. Q_s is the partition function associated with the probability of each way to construct such lattice trees, which is subject to the set N_r. The summation over the set N_r is applied to all the possible combinations of elements in N_r.

In principle Eq. (3.2) presents all the possible microstates of the system, but it has little practical use. This is because computing the right hand side of Eq. (3.2) is a tedious job. To see why this is the case, one may consider the canonical partition function of the extruding branches Q_{N_i} alone first. The lattice

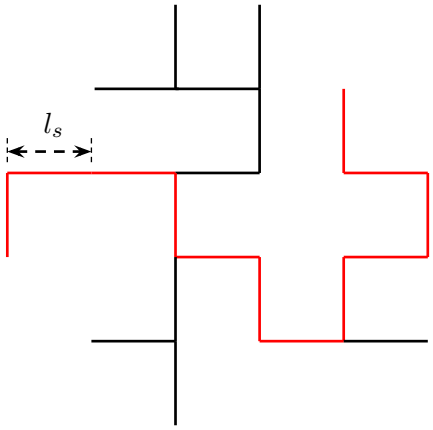

Figure 3.2: An example of lattice trees with a coordination number $z = 4$. The segments in red colour are of the linear backbone, which contains N_l segments. The black segments are of the extruding branches. In this figure, there are three such branches, i.e. $u = 3$.

tree is assumed having zero interaction energy between segments, and Q_{N_i} is simply given by the number of configurations to form these branches. The number of configurations can be computed by the following expression [Flory, 1953, p. 365]

$$\omega(N_i) = \frac{[(z-1)N_i]!}{N_i![(z-2)N_i+1]!}, \tag{3.3}$$

where $i = 1, 2, \cdots, u$. This result is based on the assumption that the segments are indistinguishable, and indeed it gives a correct value for any rooted tree provided N_i. In order to derive the partition function, computing *all* the possible configurations among the u branches is necessary. As for the backbone, Q'_{N_l} may be assumed to have a Gaussian distribution [Doi and Edwards, 1986] since the excluded volume interactions are neglected, so that

$$Q'_{N_l}(r) \propto (z-1)^{N_l} \exp\left(-\frac{3r^2}{2N_l l_s^2}\right). \tag{3.4}$$

As it has been explained in Section 3.1, lattice trees as the analogue of ring polymers have a significant difference from the branched polymers. The branching points are not fixed in the lattice trees. This greatly complicates the calculation of Eq. (3.2) since the partition function $Q_s(N_r)$ has to include all the possible ways to form such lattice trees. The only constraint upon that is the sum of the segments needs to be N_s. Therefore, combining all the terms on the right hand side of Eq.

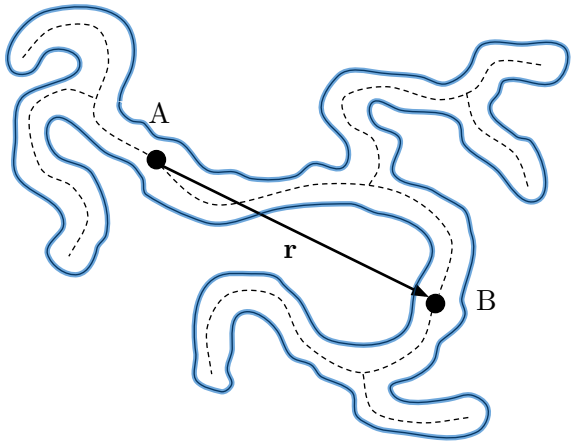

Figure 3.3: A topologically constrained ring polymers (blue solid line) resembling a lattice tree (dashed line). The surrounding obstacles are not shown in this figure. This ring polymer encloses two point-like obstacles, denoted by the circles A and B, with separation $r = |\mathbf{r}|$. The lattice tree can be deconstructed as a rooted tree attached to A and B, respectively, and a backbone section between them.

(3.2), it is too complicated to proceed to obtain equilibrium quantities such as the mean end-to-end distance of the backbone.

3.2.2 Recurrence of Branches in the Lattice Tree

Although it looks hopeless to calculate the equilibrium properties, there is a way to work around the difficult mathematics mentioned above. To study the effect of penetrations between entangled ring polymers, it is appropriate to consider the case when the contour of a ring polymer is forced to enclose two point-like obstacles with separation r. For such a lattice tree there is always a way to track a backbone section (not necessarily to be *exclusively* a linear structure) which is as a bridge to connect these two obstacles. Hence we construct the lattice tree as follows. There is a linear section, as a major part of the backbone, whose end-to-end distance is r; see Figure 3.3. The backbone is decorated by a rooted tree on each of its ends, respectively. Later we seek the grand canonical partition function of the three compartments in order to obtain the equilibrium properties of the whole lattice tree.

We first consider the grand canonical partition function Z_t of a rooted tree in the grand canonical ensemble in which the number of segments N_t is conjugated to the chemical potential. Here for the sake of simplicity we only consider the case

in which $z = 3$. The grand canonical partition function of a rooted tree is

$$Z_t(\mu) = \sum_{N_t=0}^{\infty} e^{-\alpha N_t} Q_{N_t}, \tag{3.5}$$

where μ is the chemical potential, $\alpha = -\mu/k_B T$, k_B the Boltzmann constant and T the temperature. Q_{N_t} is the canonical partition function subject to a fixed N_t. Each level of the branching can be seen as merely a linear chain attached to two rooted trees when scrutinising the rooted tree carefully. This branching process can be repeated indefinitely in the mathematical sense. Therefore a recurrence relation for Z_t can be constructed by equating the grand canonical partition function of a rooted tree to the sum of the grand canonical partition function of a linear chain and that for a tree with a linear section leading to a branch, connecting to two rooted trees; see Figure 3.4. Hence

$$\begin{aligned} Z_t &= Z_l(1 + \varepsilon Z_{t'} Z_{t''}) \\ &= Z_l(1 + \varepsilon Z_t^2), \end{aligned} \tag{3.6}$$

where the prime and double-prime denote the partition functions being of different parts of the rooted tree, ε is the fugacity associated with the three-fold branching and

$$Z_l = \sum_{N_l=0}^{\infty} e^{-\alpha N_l} Q_{N_l}, \tag{3.7}$$

the grand partition function of a linear chain. The canonical partition function Q_{N_l} is relatively simple due to the strict ways to form a linear chain and, as a result, $Q_{N_l} \sim \exp(N_l \ln 2)$. To simplify the calculation below, we let the orientational freedom $\ln 2$ be absorbed within α.

Here we are interested in the regime of large N_s limit, i.e. $N_s \gg 1$. Hence we expect $\langle N_l \rangle \gg 1$ so that we may also treat N_l as a continuous variable. The summation over N_l then can be replaced by an integral, and Eq. (3.6) becomes

$$Z_t = \frac{1}{\alpha}\left(1 + \varepsilon Z_t^2\right). \tag{3.8}$$

The sensible solution of Eq. (3.8) is

$$Z_t = \frac{1}{2\varepsilon}\left(\alpha - \sqrt{\alpha^2 - 4\varepsilon}\right), \tag{3.9}$$

because when $\varepsilon \to 0$, which corresponds to a chain without branching, the other

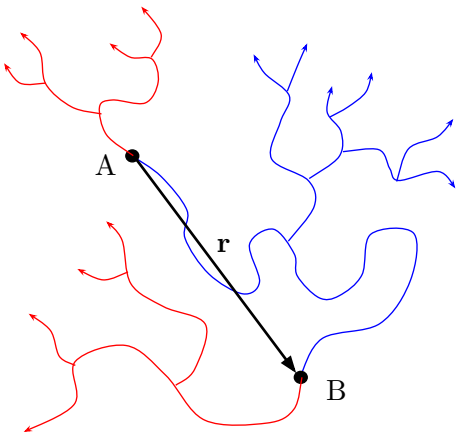

Figure 3.4: A lattice tree like the one shown in Figure 3.3 can be studied by considering the recurrence relationship of branching structure. The enclosed obstacles A and B divide it into a backbone section (blue lines) and two rooted trees (red lines). The arrows represent that the branching structure can continue indefinitely.

solution diverges and contradicts the assumption of small ε.

The other structure present in the compact lattice tree is the backbone, extending a distance r, decorated with rooted trees. The grand canonical partition function of the backbone is

$$Z_b(\mu, \mathbf{r}) = \sum_{N_b=0}^{\infty} e^{-\alpha N_b} Q_{N_b}(\mathbf{r}), \tag{3.10}$$

where Q_{N_b} is the canonical partition function subject to a fixed N_b, the number of segments in the backbone, and the vector $\mathbf{r}$ pointing from one end to the other. Eq. (3.10) can be rewritten by a Laplace transform via the force $\mathbf{f}$ acting on the backbone as the field conjugated to $\mathbf{r}$ as follows:

$$Z_b(\mu, \mathbf{f}) = \sum_{N_b=0}^{\infty} e^{-\alpha N_b} \int d\mathbf{r}\ \exp\left(\frac{-\mathbf{f}\cdot\mathbf{r}}{k_B T}\right) Q_{N_b}(\mathbf{r}). \tag{3.11}$$

A recurrence relation for the backbone can be constructed in a similar way as that for the rooted tree above. We identify the grand canonical partition function of the backbone as equal to the sum of that for a linear chain and a linear chain connected to a two-fold branch that spawns a rooted tree on one branch and a continuation of

the backbone on the other. Therefore

$$Z_b(\mu, \mathbf{f}) = \sum_{N_b=0}^{\infty} e^{-\alpha N_b} \int d\mathbf{r} \ \exp\left(\frac{-\mathbf{f}\cdot\mathbf{r}}{k_B T}\right) G_{N_b}(\mathbf{r})[1 + 2\varepsilon Z_b(\mu, \mathbf{f}) Z_t(\mu)], \tag{3.12}$$

where Z_t is the grand canonical partition function of the decorating rooted tree. Again the linear section is assumed to follow the Gaussian distribution so that

$$G_{N_b}(\mathbf{r}) = \left(\frac{3}{2\pi N_b l_s^2}\right)^{3/2} \exp\left(-\frac{3\mathbf{r}^2}{2N_b l_s^2}\right) \tag{3.13}$$

with $G_{N_b}(\mathbf{r})$ being subject to the number of segments in the backbone section N_b.

In the Cartesian coordinates, $\mathbf{f} \equiv (f_1, f_2, f_3)$ and $\mathbf{r} \equiv (r_1, r_2, r_3)$, and the integral in Eq. (3.12) can be calculated as follows:

$$\begin{aligned}
&\prod_{i=1}^{3} \int_{-\infty}^{\infty} dr_i \ \exp\left(\frac{-f_i r_i}{k_B T}\right) G_{N_b}(r_i) \\
&= \prod_{i=1}^{3} \int_{-\infty}^{\infty} dr_i \ \exp\left(\frac{-f_i r_i}{k_B T}\right) \times \left(\frac{3}{2\pi N_b l_s^2}\right)^{1/2} \exp\left(\frac{-3r_i^2}{2N_b l_s^2}\right) \\
&= \prod_{i=1}^{3} \left(\frac{3}{2\pi N_b l_s^2}\right)^{1/2} \int_{-\infty}^{\infty} dr_i \ \exp\left[-\left(\frac{f_i r_i}{k_B T} + \frac{3r_i^2}{2N_b l_s^2}\right)\right] \\
&= \prod_{i=1}^{3} \exp\left(\frac{N_b l_s^2 f_i^2}{6k_B^2 T^2}\right) \\
&= \exp(N_b k^2),
\end{aligned} \tag{3.14}$$

where $k^2 = k_1^2 + k_2^2 + k_3^2$ and $k_i = l_s f_i / \sqrt{6} k_B T$, $i = 1, 2$ and 3. This new variable k is a dimensionless energy associated with the force $\mathbf{f}$. Again we expect $\langle N_b \rangle \gg 1$ so that N_b is treated as a continuous variable, and Z_b becomes

$$Z_b = \sum_{N_b=0}^{\infty} e^{-(\alpha - k^2)N_b}(1 + 2\varepsilon Z_b Z_t) = \frac{1}{\alpha - k^2}(1 + 2\varepsilon Z_b Z_t). \tag{3.15}$$

This equation can be solved without any difficulty and the solution is

$$Z_b = \left(\alpha - k^2 - 2\varepsilon Z_t\right)^{-1} = \frac{1}{\sqrt{\alpha^2 - 4\varepsilon} - k^2}. \tag{3.16}$$

The grand canonical partition function for the entire lattice tree, constrained to only cover a distance r via the applied force $\mathbf{f}$, is therefore the product of the grand

canonical partition function of the backbone and that for a rooted tree at each end of the backbone. Consequently it is expressed as

$$Z(\mu, k) = Z_b(\mu, k) Z_t(\mu)^2. \tag{3.17}$$

3.2.3 Statistical Properties of the Lattice Tree

The average number of segments in the rooted tree can be calculated via $Z_t(\mu)$ by

$$\langle N_t \rangle = -\frac{\partial}{\partial \alpha} \ln Z_t = \frac{-1}{Z_t} \frac{\partial Z_t}{\partial \alpha} = \frac{1}{\sqrt{\alpha^2 - 4\varepsilon}}. \tag{3.18}$$

Likewise, the average number of segments in the trunk can be calculated via $Z_b(\mu, k)$ as follows:

$$\langle N_b \rangle = \frac{-1}{Z_b} \frac{\partial Z_b}{\partial \alpha} = \frac{\alpha}{\sqrt{\alpha^2 - 4\varepsilon} \left(\sqrt{\alpha^2 - 4\varepsilon} - k^2 \right)} \tag{3.19}$$

Considering the case of no applied force such that $k = 0$ and anticipating $\langle N_b \rangle \gg 1$ due to $N_s \gg 1$, one can further write $\alpha = \alpha_c + \delta\alpha$, where $\alpha_c^2 = 4\varepsilon$ and $\delta\alpha \ll \alpha_c$, to show that

$$\delta\alpha = \frac{1}{4\varepsilon^{1/2} \langle N_t \rangle^2} \tag{3.20}$$

and

$$\delta\alpha = \frac{1}{2\langle N_b \rangle} \tag{3.21}$$

according to Eqs. (3.18) and (3.19). Eqs. (3.20) and (3.21) suggest that in equilibrium $\langle N_t \rangle \sim \varepsilon^{-1/4} \langle N_b \rangle^{1/2}$. Thus if anticipating that most of the segments lie in the decorated backbone, one can write $\delta\alpha = 1/2N_s$ and thus $\langle N_t \rangle \sim \varepsilon^{-1/4} N_s^{1/2}$.

The components of the average end-to-end distance of the backbone section can be computed from the normalised first moment

$$\langle \Delta r_b \rangle_i = \frac{\sum_{N_b=0}^{\infty} e^{-\alpha N_b} \int d\mathbf{r}\; r_i \exp\left(-\mathbf{f} \cdot \mathbf{r} / k_B T\right) Q_{N_b}(\mathbf{r})}{\sum_{N_b=0}^{\infty} e^{-\alpha N_b} \int d\mathbf{r}\; \exp\left(-\mathbf{f} \cdot \mathbf{r} / k_B T\right) Q_{N_b}(\mathbf{r})}. \tag{3.22}$$

By noticing $k_i = l_s f_i / \sqrt{6} k_B T$, $i = 1, 2$ and 3, one can write the above equation as

$$\langle \Delta r_b \rangle_i = \frac{-l_s}{\sqrt{6}} \frac{1}{Z_b} \frac{\partial Z_b}{\partial k_i} = \frac{-2 l_s}{\sqrt{6}} \frac{k_i}{\sqrt{\alpha^2 - 4\varepsilon} - k^2}. \tag{3.23}$$

Indeed if there is no force applied to the backbone, the average end-to-end distance becomes zero as expected.

On the other hand, the first non-vanishing moment when the force vanishes is the second moment,

$$\langle \Delta r_b^2 \rangle_i = \frac{\sum_{N_b=0}^{\infty} e^{-\alpha N_b} \int d\mathbf{r}\; r_i^2 \exp\left(-\mathbf{f}\cdot\mathbf{r}/k_BT\right) Q_{N_b}(\mathbf{r})}{\sum_{N_b=0}^{\infty} e^{-\alpha N_b} \int d\mathbf{r}\; \exp\left(-\mathbf{f}\cdot\mathbf{r}/k_BT\right) Q_{N_b}(\mathbf{r})}. \tag{3.24}$$

Hence the second moment can be easily calculated by

$$\langle \Delta r_b^2 \rangle_i = \frac{l_s^2}{6}\frac{1}{Z_b}\frac{\partial^2 Z_b}{\partial k_i^2} = \frac{l_s^2}{3}\left[\frac{4k_i^2 - k^2 + \sqrt{\alpha^2 - 4\varepsilon}}{(\sqrt{\alpha^2 - 4\varepsilon} - k^2)^2}\right]. \tag{3.25}$$

With the limit in which $k \to 0$ one obtains the mean-squared end-to-end distance of the backbone section

$$\lim_{k\to 0}\langle \Delta r_b^2 \rangle = \lim_{k\to 0}\sum_{i=1}^{3}\langle \Delta r_b^2 \rangle_i = l_s^2\left(\alpha^2 - 4\varepsilon\right)^{-1/2}. \tag{3.26}$$

Following Eqs. (3.20) and (3.21) one has

$$\langle \Delta r_b^2 \rangle_{eq} = \lim_{k\to 0}\langle \Delta r_b^2 \rangle = \frac{l_s^2}{2}\varepsilon^{-1/4}\delta\alpha^{-1/2} = \frac{\sqrt{2}}{2}\varepsilon^{-1/4}\langle N_b \rangle^{1/2} l_s^2. \tag{3.27}$$

As a result, the root mean-squared end-to-end distance of the backbone section is proportional to $\langle N_b \rangle^{1/4}$.

3.3 Characteristics of Lattice Trees

3.3.1 Overlap Concentrations and Density of Lattice Trees

Eq. (3.27) shows the root mean-squared end-to-end distance of the backbone $R_b = \langle \Delta r_b^2 \rangle_{eq}^{1/2} \sim \langle N_b \rangle^{1/4} l_s$. If one assumes that this part of lattice tree contains most segments of the whole and $N_s \gg 1$, one expects that $R_b \propto N_s^{1/4}$. This leads to an over-packed tree whose density diverges as $N_s \to \infty$. Nevertheless, this result does not devastate the theoretical model we have built so far.

The statistical weight of branching is associated with the branching fugacity ε. This can be seen to originate from the energy cost of bending the polymer chains to create a branching between dense surrounding chains. Therefore, we expect ε and thus R_b are related to the stiffness of the ring polymer. The appropriate parameter to present the stiffness of a polymer chain is its persistence length l_p. As

we will explain below, the prefactor of R_b becomes important when the ratio of the persistence length and the diameter of polymer chains d is very high, i.e. $l_p/d \gg 1$. This condition corresponds to the case of semiflexible polymers.

Furthermore, the phantom chain approximation could be reasonable if the system is above the semidilute regime $C \gg C^\star$, where C is the concentration of polymers and the overlap concentration $C^\star \sim R_b^{-3}$. In such a regime, the excluded volume interactions is known to be screened. Here we are interested in seeing whether the conditions with ring penetrations are accessible in experiments. Essentially we have to examine whether a ring fully occupies a volume $V \sim R_b^3$ within the range of concentrations which interests us.

By reviewing the model we have discussed so far, it is clear that the segment length l_s can be related to the persistence length l_p. It can be proved that $l_s = 2l_p$ in the case of long, flexible linear polymers ($L \gg l_p$), and l_s is called the Kuhn length [Grosberg and Khokhlov, 1994]. In this work l_s is a unit length scale corresponding to a duplex polymer strands of the ring polymer, and l_s is of the same order as l_p. For the sake of convenience in the discussion below, we will ignore the prefactor and just replace l_s by l_p. The volume fraction of a single chain within its own coil volume, namely the volume fraction corresponding to $C^\star$, is estimated with the result from Eq. (3.27) so that

$$\phi^\star \sim \frac{N_s d^2 l_p}{(\varepsilon^{-1/8} N_s^{1/4} l_p)^3} = \varepsilon^{3/8} N_s^{1/4} \left(\frac{d}{l_p}\right)^2, \tag{3.28}$$

where d is the diameter of a chain. We speculate that the penetrating ring polymers need to be (i) highly overlapping with neighbouring chains, (ii) having many neighbours with which they can be threaded and (iii) not exceeding the maximum concentration of the melt limit, $\phi \approx 1$. As a result, the volume fraction of the ring polymers has to be $\phi^\star \ll \phi \lesssim 1$. We are reassured that, according to Eq (3.28) and $\varepsilon \to 1$ (the branching limit), $\phi^\star$ does not reach the order of unity for semiflexible polymers, such as DNA, until $N_s \gtrsim \mathcal{O}(10^8)$.

3.3.2 Effects of Stiffness on the Branching

As explained above, the branching of such lattice trees at high concentrations are controlled via the fugacity ε, which is related to the stiffness of the polymer chain. Here we are going to examine the energy cost associated with the bending of chains

near the branch. The fugacity ε can be expressed as

$$\varepsilon = \exp\left(\frac{-E}{k_B T}\right), \tag{3.29}$$

where E is the bending energy associated with the reorientation of the polymer chains to make a branch. With a higher concentration, the energy cost of making a branch becomes much higher since there are more neighbouring chains to be pushed away in order to make enough space to accommodate the branch.

One simple way to proceed the calculation is to consider the bending energy of making a branch in an array of fixed obstacles, where our representation of lattice trees is exact. This corresponds to the case of a ring polymer in a gel, which has a bulk modulus of the order of $K \sim k_B T/l_e^3$. Moreover, in order to make a branch between the entangled ring polymers, it involves a distortion of the neighbouring chains with a volume of the order $\hat{r}^3$. Assuming the duplex polymer chains within the tube push away the surrounding chains near the branch, the bending chains near the branch must have a radius of curvature $\hat{r}$. The energy of branching therefore is of the order of

$$E \sim k_B T \left[\frac{l_p}{\hat{r}} + \left(\frac{\hat{r}}{l_e}\right)^3\right]. \tag{3.30}$$

The second term in the bracket arises from the fact that the bending chains have to compress against the neighbouring chains, of which the energy cost is associated with the bulk modulus. Here we consider a regime where $l_e < l_p$, and $\hat{r}$ is of the same order of l_p. As a result, the cubic term in Eq. (3.30) is dominant in the bending energy. Expecting the penetrating rings to have a cost of bending, $E/k_B T \gg 1$, the fugacity will be $\varepsilon \ll 1$. For a long ring polymer, which has been considered in this model, one expects $1 \ll N_s \ll N'$, where N' corresponds to the the volume fraction that is limited by $\phi \lesssim 1$, so that

$$1 \ll N_s \ll \left(\frac{l_p}{d}\right)^8 \varepsilon^{-3/2}. \tag{3.31}$$

According to the condition $\varepsilon \ll 1$ and Eq. (3.31), one can estimate the limits of the fugacity required in experiments in order to observe penetrating ring polymers. If plotted on the N_s-ε phase space, the boundaries of the conditions should be $N_s > 1$, $\varepsilon < 1$ and $\varepsilon < (l_p/d)^{16/3} N_s^{-2/3}$. This is shown in Figure 3.5.

Furthermore, with Eq. (3.20) and $\delta\alpha = 1/2N_s$, one obtains the number of

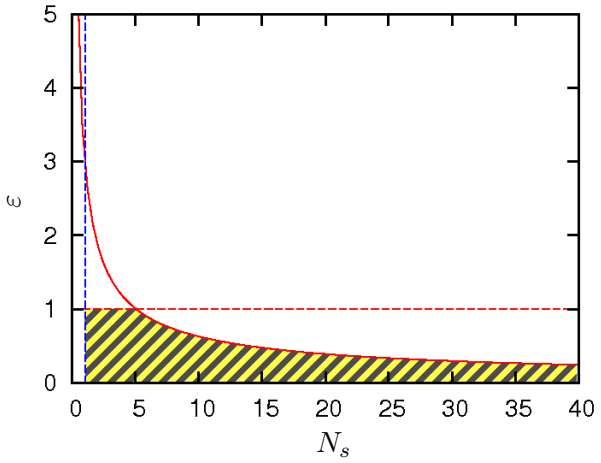

Figure 3.5: A diagram showing the N_s-ε phase space. The yellow-black pattern indicates the region where ε and N_s are relevant to the scenario of penetrating ring polymers. The curve (red solid line) is $\varepsilon = 3.0 \times N_s^{-2/3}$, which corresponds to $l_p/d \approx 1.23$.

segments in the rooted tree as

$$\langle N_t \rangle \gtrsim \left(\frac{d}{l_p}\right)^{4/3} N_s^{2/3}. \tag{3.32}$$

This is consistent with our previous assumption that most of the segments lie in the decorated backbone. In fact, if one examines Eq. (3.12) carefully, it is obvious that most of the segments are part of the linear section of the backbone. In other words, the ring looks more like a linear object with some relatively small branches extruding from the linear part. This finding will be the main topic of the next chapter, and we will exploit it to calculate the dynamics of penetrating ring polymers. Another important result obtained from the fugacity limits is that

$$\langle \Delta r_b^2 \rangle_{eq} \gtrsim \left(\frac{d}{l_p}\right)^{4/3} N_s^{2/3} l_p^2; \tag{3.33}$$

see Eq. (3.27). Hence the root mean-squared end-to-end distance of the backbone R_b has a scaling with N_s as $R_b \propto N_s^{1/3}$.

Chapter 4

The Stress Relaxation of Penetrating Loop Strands

As we have discussed in Chapter 3, the mass distribution predominantly falls into the backbone section. This is consistent with the assumption that the penetration events are in a perturbative sense. A further simplified model was built by ignoring the branching such that each ring polymer resembled a loop strand. Our approach involved several simplifying assumptions that mitigated the ring penetration problem. This model of penetrating loop strands then was analysed by following the Doi-Edwards tube model. Subsequently the resulting coarse-grained model was employed in the Monte Carlo simulation. The simulation clearly demonstrated the slowing of dynamics caused by the penetrations. These simulation data and their implications on experiments will be discussed in Chapter 6.

4.1 Entangled Loop Strands

4.1.1 Ideal Chains

Based on the analysis in Section 3.3, a simpler model of entangled ring polymers can be made by adopting the ansatz that the ring polymer *compactifies* in such a way as to form a duplex structure in which each tube segment [Cates and Deutsch, 1986] contains an outgoing and a returning segment of the ring polymer; see Figure 4.1. The effective length of the tube is reduced by a factor of two if assumed ideal [Zimm and Stockmayer, 1949], but the chain is now guaranteed to satisfy its topological constraints and remains unknotted.

This represents an explicit set of microscopic configurations that can be shown to satisfy all the topological constraints rigorously. This set may fail to include

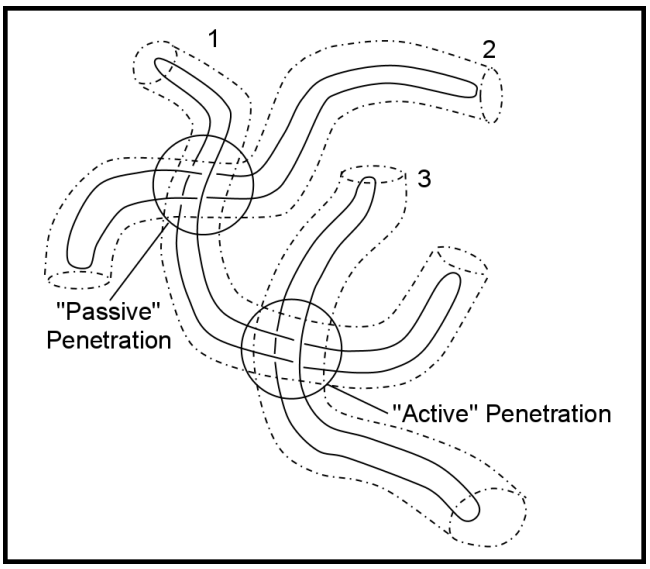

Figure 4.1: A schematic diagram showing three unbranched, compactified ring polymers (solid curves) and the tubes (dash-dotted curves) provided by their entanglements with a background gel and/or neighbouring rings (not shown). The labels identify the nature of penetrations on Polymer 1.

some equilibrium chain states in the melt, where the duplex structure may permit penetration *between* the duplex pair (violating compactification) and be branched. However, it is the primary aim of this research to study the effect of such penetrations perturbatively (where they remain rare). While one can also suppress the branching by setting the mesh size of the background gel or neighbouring rings to be much smaller than the persistence length of the chain, it is anyway natural to study the unbranched limit first. It is likely that the onset of the topological glass transition that we describe below will be shifted if we permit branched structures, e.g., removing the background gel or choosing one with a large mesh size. However, it is difficult to see how its *existence* could be affected by branching. The novelty of our approach lies in the way in which we account for penetration events; see Figure 4.1. These do not violate topological constraints and can be thought of as a perturbative relaxation of the compact chain ansatz introduced above.

In Figure 4.1, the labels identify the nature of penetrations on Polymer 1. Here Polymer 2 has actively penetrated Polymer 1, creating an associated passive penetration in the corresponding tube segment of Polymer 1. Polymer 3 has been penetrated by Polymer 1, resulting in a passive penetration to Polymer 3 and an active penetration to Polymer 1. The passive penetration on Polymer 1 will remain until one end of Polymer 2 has diffused through that tube segment. Until that

happens the motion of Polymer 1 is restricted by this penetration, which prevents either end diffusing through this tube segment. The active penetration on Polymer 1 will be lost as soon as either of its ends moves through the tube segment containing this penetration, simultaneously annihilating the corresponding passive penetration on Polymer 3.

4.1.2 Fluctuation, Length Defects and Reptation

Before discussing the detailed calculation of the penetrating loop strands, it is instructive to review the most successful mean-field model of entangled linear polymers. As proposed by de Gennes [1971], the fundamental relaxation mode of an entangled linear polymer is believed to be the propagation of *kink gas*, a series of non-interacting length defects, along the polymer chain; see Figure 4.2. This is based on the concept that the non-crossing constraints imposed by the surrounding chains prevent a chain laterally moving through them. The length defects hence tend to move randomly along a curvilinear path, which is correlated to the tube-like confinement of the surrounding chains. The random motion of these length defects, of course, originates from the thermal fluctuation of the length and the conformation of the polymer chain itself.

Later Edwards refined this concept and built a detailed analytic model (now often referred to the Doi-Edwards tube model) to describe such processes. The most important result of this model is the disengagement time,

$$\tau_d^{(0)} = \frac{\zeta_0 N^3 b^4}{\pi^2 k_B T a^2}, \tag{4.1}$$

where ζ_0 is the friction constant of a monomer, N the degree of polymerisation, b the bond length and a the tube width. This is the time needed for a primitive chain, the statistical representation of a confined polymer, to disengage from the original tube it was confined to at $t = 0$. Notice that the parameter a is of the order of the mesh size of surrounding chains, which is approximately the entanglement length l_e [Doi and Edwards, 1986]. In later discussions this disengagement time is rescaled by $\zeta_0 \to \zeta$, $N \to N_s$ and $Nb^2/a \to L_c$, where ζ is the friction constant of a segment, N_s the number of segments and L_c the contour length of a primitive chain. The rescaled disengagement time can be seen as a special case without penetration of primitive chains involved, therefore it is denoted as $\tau_d^{(0)}$ to stress the fact that there is no penetration.

It is noticeable that, as shown in Figure 4.1, the ring polymers have no chain end to relax length defects as that in the Doi-Edwards tube model. This is one of

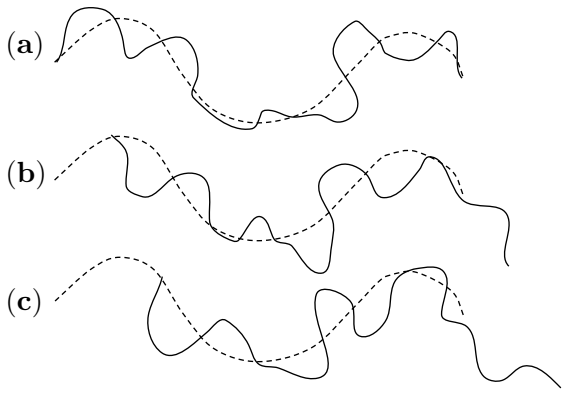

Figure 4.2: The tube model describes the relaxation process of entangled linear polymers as follows. Each polymer can only move along a curvilinear path—the primitive path (dashed lines)—due to the constraints of neighbouring chains. The kinks, also called the length defects, randomly diffuse along the path until them move to the ends. The fluctuation at the ends also creates new kinks simultaneously. The chain ends essentially explore new paths toward random directions, see (**a**)–(**c**), and eventually the whole chain disengages from the original primitive path. In this figure the tube is not shown.

the reasons why many see developing analytic models for entangled ring polymers as a challenge in polymer physics. Without the chain ends, the most accessible mean-field theory seems to have no way to describe the dynamics of ring polymers. However, in certain conditions, the fluctuation of the length and the conformation should still provide a similar relaxation mode to that of reptation. Combined with the discussion in Chapter 3, it is possible for highly entangled ring polymers to be modelled as linear objects with relaxation via a form of reptation. In this chapter, we will demonstrate a simple model of penetrating loop strands which is built on the basis of the Doi-Edwards tube model.

4.2 Obstructed Reptation

4.2.1 Tube Model with Obstructions

Let s_n be the curvilinear coordinate of the n-th segment of primitive chain measured from a fixed point on the tube so that the contour length of the primitive chain $L_c = |s_{N_s} - s_0|$, where N_s is the number of segments in the primitive chain. In this thesis the length between two segments is assumed to be constant. This is a valid

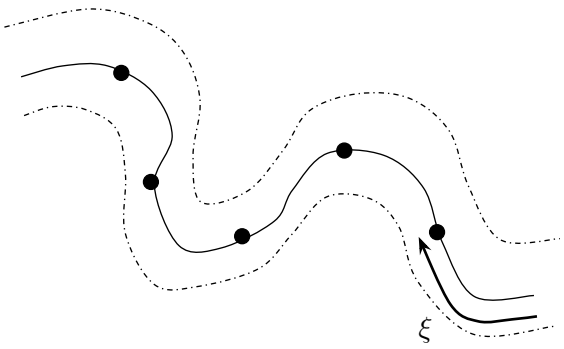

Figure 4.3: A primitive chain (solid line) confined in a tube (dash-dot lines). The contour length of this primitive chain is L_c, including N_s segments. In the obstructed reptation, the motion of chain ends is blocked by the passive penetrations (closed circles) along the primitive path. In this figure, the right end moves a distance ξ to meet the nearest passive penetration. Each passive penetration can be viewed as a wall which forces the chain ends bouncing back and forth, until the associated penetrating chain moves away from the primitive path.

assumption for $N_s \gg 1$ since the contour length fluctuation is negligible compared to L_c [Doi and Edwards, 1986]. As a result, the dynamics of the whole primitive chain can be easily depicted by the motion of its centre of mass.

To describe the stress relaxation of the loop strand, or its self-diffusion within the tube, a random force exerted upon the centre of mass may be explicitly expressed in an equation of motion. The dynamics of the centre of mass of the primitive chain can be described by the Langevin equation

$$\zeta_c \frac{\partial}{\partial t} s_c(t) = -\frac{\partial}{\partial s} \left[U_p(s_0, t) + U_p(s_{N_s}, t) \right] + f_c(t), \tag{4.2}$$

where s_c is the position of the centre of mass. f_c is the random force acting on the centre of mass and characterised by the moments $\langle f_c(t) \rangle = 0$ and $\langle f_c(t) f_c(t') \rangle = 2\zeta_c k_B T \delta(t - t')$. The constant ζ_c is the effective friction constant of the centre of mass and $\zeta_c = N_s \zeta$, where ζ is the friction constant of a single segment.

In Eq. (4.2) the potential $U_p(s, t)$ is zero everywhere except where there is a passive penetration in the tube. The form of U_p can be arbitrary as long as it is localised and has a large magnitude to prevent chain ends passing through. For example, a Gaussian function with a small width can be such a potential. In real cases there could be multiple passive penetrations in a tube, so U_p should

be a convolution of Gaussian function and delta functions along the coordinate s. Nevertheless, the potential U_p only matters when one of the two ends is close to the position at which it has a non-zero value.

An alternative approach is to consider the Smoluchowski equation of the probability function $\Psi(\xi, t; s)$, which is the probability that the primitive chain moves the distance ξ while its ends have not reached the position s of the original tube [Doi and Edwards, 1986]. The equation is written as

$$\frac{\partial \Psi}{\partial t} = \frac{\partial}{\partial \xi} \frac{1}{N_s \zeta} \left(k_B T \frac{\partial \Psi}{\partial \xi} + \frac{\partial U_p'(\chi_p, t)}{\partial \xi} \Psi \right), \tag{4.3}$$

where $U_p'(\chi_p, t)$ is a function of $\chi_p \equiv \{\chi_1, \chi_2, \cdots, \chi_m\}$, the curvilinear coordinates of obstructions formed by penetrations. Like U_p in Eq. (4.2), U_p' plays the role as potential barriers to prevent $\Psi(\xi, t; s)$ spreading toward certain directions along the tube. U_p' is also localised so that Eq. (4.3) will be equivalent to a diffusion equation before the ends reaching any of χ_p.

Unfortunately, both Eqs. (4.2) and (4.3) are difficult to handle, because the potential U_p and U_p' are not just localised but also time-dependent. It is easy to see the difficulty by imagining several chains penetrating each other and maintaining the equilibrium; the average number of active or passive penetrations per chain remains constant for a very long time compared to the time scale of observation. The only way to relax a passive penetration is to move the penetrating chain away from the corresponding active penetration. The motion of this penetrating chain is also constrained by the passive penetrations on its own primitive path. Therefore both U_p and U_p' have to be realised within a self-consistent framework, and the mathematics to express them would be complicated. Instead of deriving U_p and U_p' directly, we consider fixed obstacles in the next subsection and study the more general problem of time-varying penetrations by a Monte Carlo simulation in Section 4.3.

4.2.2 Permanent Obstacles

As explained above, Eq. (4.3) is equivalent to a diffusion equation as long as the ends do not reach any of χ_p before reaching an arbitrary segment s. For an instructive purpose, the obstructed reptation model discussed above can be simplified if the penetrations are static. Since the ends cannot pass through these penetrations, only the two outermost penetrations affect the dynamics of this primitive chain. Consider that the same tube picture explained in Subsection 4.2.1 now contains only two permanent obstacles inside the tube, denoted by their curvilinear coordinates χ_1

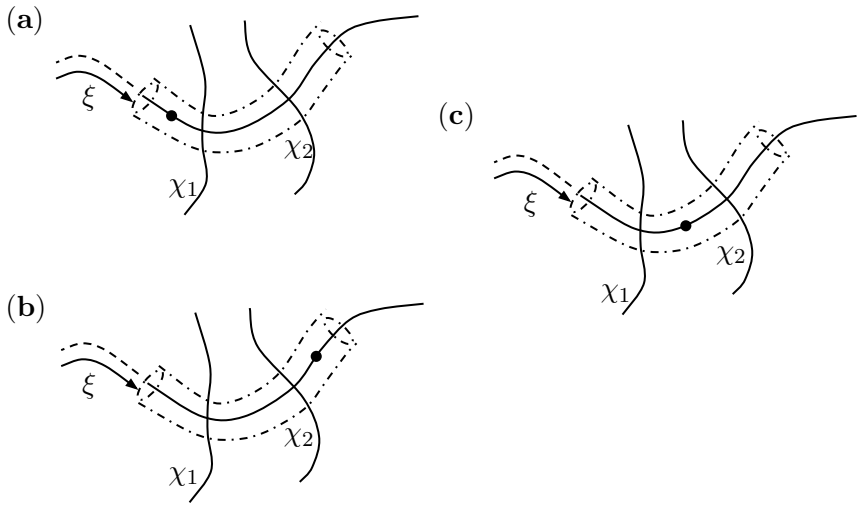

Figure 4.4: The tube with two permanent obstacles χ_1 and χ_2 inside. The black dots represent the arbitrary segment s in the calculation.

and χ_2 ($\chi_2 > \chi_1$), at which the ends of primitive chain cannot pass. The ends of the primitive chain, in fact, will never be anywhere between χ_1 and χ_2. It is obvious that the remaining length of the original tube will be $\chi_2 - \chi_1$ as $t \to \infty$.

By applying the method of images to Eq. (4.3), the potential U_p' can be discarded. Instead, appropriate boundary and initial conditions are used to generate the same solutions of the original differential equation. On the one hand, the obstacles are effectively *hard* walls which stop $\Psi(\xi, t; s)$ further spreading through them. On the other, the arbitrary segment s is a *soft* boundary at which $\Psi(\xi, t; s)$ becomes zero when one of the ends reaches s. Hence one can generate solutions by using the method of images and including appropriate image sources of the probability function $\Psi(\xi, 0; s)$ at time $t = 0$; see Figure 4.5. These sources need to be in the same magnitude and symmetric or anti-symmetric, i.e. sign reversed, with respect to the hard boundaries or the soft ones, respectively. In this way $\Psi(\xi, t; s)$ maintains a finite value at the obstacles and vanishes at the segment s after a certain time interval. The time evolution of the probability function $\Psi(\xi, t; s)$ now is described by the diffusion equation

$$\frac{\partial \Psi}{\partial t} = D \frac{\partial^2 \Psi}{\partial \xi^2}. \tag{4.4}$$

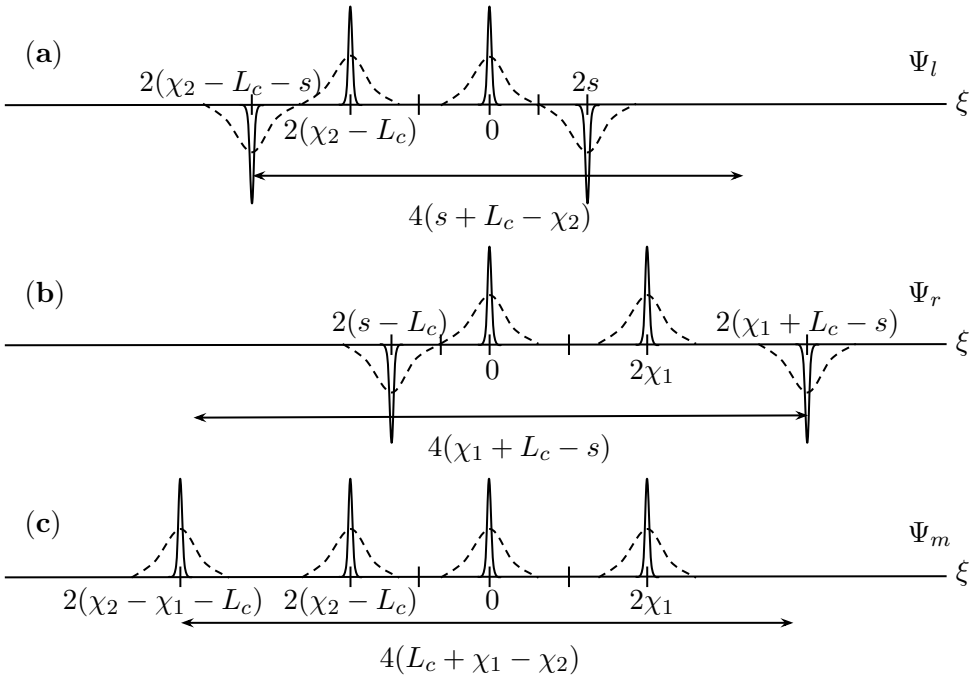

Figure 4.5: A schematic diagram showing the initial conditions (peaks in solid lines) for Ψ_l, Ψ_r and Ψ_m (from top to button), respectively. The dashed lines show the probability functions some time after $t = 0$. The two-sided arrows indicate the period of each probability function.

The diffusion constant is given by $D = k_B T/N_s\zeta$. The general solution of Eq. (4.4) can be written in such a form

$$\Psi(\xi, t; s) = A_0 + \sum_{q=1}^{\infty} \left(A_q \cos \frac{q\pi\xi}{2L_i} + B_q \sin \frac{q\pi\xi}{2L_i} \right) \exp\left(\frac{-q^2 t}{\tau_{s;L_i}} \right), \tag{4.5}$$

where L_i is the period of Ψ and $\tau_{s;L_i} = 4L_i^2/D\pi^2$. Latter the initial and boundary conditions will determine the coefficients A_0, A_q and B_q. For a tube segment s to remain at time t, the chain can have moved a distance ξ between arbitrary values a and b so that

$$\psi(s, t) = \int_a^b d\xi \; \Psi(\xi, t; s) \tag{4.6}$$

gives the probability that the segment s remains at time t. In the picture of obstructed reptation with permanent obstacles, the chain is divided into three parts by χ_1 and χ_2. We will present the derivation of Ψ and ψ for the separated three parts below.

For an arbitrary segment s that $s < \chi_1$, as shown in Figure 4.4 (**a**), the corresponding probability function Ψ_l is

$$\Psi_l = \sum_{q=1}^{\infty} \frac{-1}{L_l} \left[\sin \frac{q\pi s}{2L_l} + \sin \frac{q\pi(s + 2L_c - 2\chi_2)}{2L_l} \right] \sin \frac{q\pi(\xi - s)}{2L_l} \exp\left(\frac{-q^2 t}{\tau_{s;L_l}} \right), \quad (4.7)$$

where $L_l = s + L_c - \chi_2$. Hence the probability that the tube segment s (where $s < \chi_1$) is remaining at time t is

$$\begin{aligned} \psi_l = \int_{\chi_2 - L_c}^{s} d\xi \; \Psi_l &= \sum_{q=1}^{\infty} \frac{2}{q\pi} \left[\sin \frac{q\pi s}{2L_l} + \sin \frac{q\pi(s + 2L_c - 2\chi_2)}{2L_l} \right] \times \\ &\quad \left[1 - \cos \frac{q\pi(s + L_c - \chi_2)}{2L_l} \right] \exp\left(\frac{-q^2 t}{\tau_{s;L_l}} \right). \end{aligned} \quad (4.8)$$

Similarly for an arbitrary segment s that $s > \chi_2$, as shown in Figure 4.4 (**b**), the corresponding probability function Ψ_r is

$$\Psi_r = \sum_{q=1}^{\infty} \frac{1}{L_r} \left[\sin \frac{q\pi(L_c - s)}{2L_r} + \sin \frac{q\pi(L_c - s + 2\chi_1)}{2L_r} \right] \sin \frac{q\pi\xi}{2L_r} \exp\left(\frac{-q^2 t}{\tau_{s;L_r}} \right), \quad (4.9)$$

where $L_r = \chi_1 + L_c - s$. The probability that this tube segment s (where $s > \chi_2$) is remaining at time t is

$$\begin{aligned} \psi_r = \int_{s - L_c}^{\chi_1} d\xi \; \Psi_l &= \sum_{q=1}^{\infty} \frac{-2}{q\pi} \left[\sin \frac{q\pi(L_c - s)}{2L_r} + \sin \frac{q\pi(L_c - s + 2\chi_1)}{2L_r} \right] \times \\ &\quad \left[\cos \frac{q\pi(\chi + L_c - s)}{2L_r} - 1 \right] \exp\left(\frac{-q^2 t}{\tau_{s;L_r}} \right). \end{aligned} \quad (4.10)$$

The last situation is that an arbitrary segment s falls between χ_1 and χ_2, i.e. $\chi_1 < s < \chi_2$; see Figure 4.4 (**c**). Intuitively the chain ends never reach s as both are blocked by either χ_1 or χ_2. The corresponding probability function Ψ_m is

$$\begin{aligned} \Psi_m &= \frac{1}{L_m} + \sum_{q=1}^{\infty} \frac{1}{L_m} \left[3 \cos \frac{q\pi\xi}{2L_m} - 2 \sin \frac{q\pi\chi_1}{2L_m} \sin \frac{q\pi(\chi_1 - \xi)}{2L_m} - \right. \\ &\quad \left. 2 \sin \frac{q\pi(\chi_2 - L_c)}{2L_m} \sin \frac{q\pi(\chi_2 - L_c - \xi)}{2L_m} \right] \exp\left(\frac{-q^2 t}{\tau_{s;L_m}} \right), \end{aligned} \quad (4.11)$$

where $L_m = L_c + \chi_1 - \chi_2$. The tube segment s in the middle between χ_1 and χ_2

should persist all the time, and the probability of that is expressed by

$$\begin{aligned}\psi_m &= \int_{\chi_2-L_c}^{\chi_1} d\xi\ \Psi_m \\ &= 1+\sum_{q=1}^{\infty}\frac{2}{q\pi}\left[\sin\frac{q\pi\chi_1}{2L_m}-\sin\frac{q\pi(\chi_2-L_c)}{2L_m}\right]\exp\left(\frac{-q^2t}{\tau_{s;L_m}}\right). \qquad (4.12)\end{aligned}$$

The portion of the original tube remains at time t, denoted as $\varphi(t)$, should be obtained by integrating $\psi(s,t)$ with respect to the coordinate s from 0 to L_c. Since the two penetrations separate the tube into three parts, however, one has

$$\varphi_l(t)=\frac{1}{L_c}\int_0^{\chi_1} ds\ \psi_l(s,t), \qquad (4.13)$$

$$\varphi_r(t)=\frac{1}{L_c}\int_{\chi_2}^{L_c} ds\ \psi_r(s,t) \qquad (4.14)$$

and

$$\varphi_m(t)=\frac{1}{L_c}\int_{\chi_1}^{\chi_2} ds\ \psi_m(s,t). \qquad (4.15)$$

Therefore the portion of the original tube remains at time t is given by $\varphi(t)=\varphi_l(t)+\varphi_m(t)+\varphi_r(t)$. The remaining lengths of the left and right section decrease with time, and $\varphi(t)\to(\chi_2-\chi_1)/L_c$ when $t\to\infty$ according to Eqs. (4.8), (4.10) and (4.12), as expected. The calculation above demonstrates that the effect of the penetrations is localised, only affecting the stress relaxation when the ends encounter these penetrations.

4.3 Monte Carlo Simulations

4.3.1 The Coarse-grained Tube Model

In Section 4.2 we showed that analytically computing the stress relaxation of the entangled loop strands would be a difficult task, if not impossible. When the obstacles were simplified to permanent ones, the calculation was manageable with the method of images, though it did not offer much useful insight into the dynamics. Nonetheless, the calculation demonstrated the consequence of introducing the topological constraints created by penetrations.

The direct effect of the penetrations was to stop the chain diffusing freely along the primitive path, thus the stress relaxation was hindered by these obstacles. Before the chain ends reached any of the penetrations, however, they created new sections of primitive path and reduced the length of the original tube in the same way as that in the Doi-Edwards tube model. This has been shown in Eqs. (4.8), (4.10) and (4.12). Therefore a simple phenomenological model can be built based on this observation.

To build such a phenomenological model, the first challenge is to integrate the effect of the penetration into the model. Indeed the free energy (or statistical weight) associated with these penetration events is difficult to calculate and likely depends on the monomer density and persistence length l_p. We do not attempt to compute this from first principles, as explained in Section 4.2, but rather define a parameter p to be the probability that the primitive path of a duplex chain penetrates a neighbouring ring on moving one entanglement length. Provided p is non-zero one always expects many penetrations in the large N_s limit. As it will be shown below, the onset of the transition to the glassy state occurs when the number of penetrations *per ring* is only of order unity and should therefore be physically accessible.

Here and in what follows we make the system coarse-grained on the scale of the entanglement length l_e. Thus N_s represents the number of entanglement lengths along the duplex ring polymer tube. When employing such a model into a numerical simulation, this is a significant advantage over microscopically detailed models, speeding up the computation by orders of magnitude. We then can study the curvilinear diffusion of the primitive chain within the tube formed by entanglements provided by its neighbours. In this model the system is directly controlled by only two parameters, the entanglement length l_e and the penetration probability p. Since we are interested in how the chain relaxes from a tube with the additional constraints of penetrations, we will only focus on the penetration probability p. Hereafter l_e will merely play the role of a length unit.

4.3.2 The Monte Carlo Experiment

As we have discussed in Section 4.2, studying the dynamics of entangled loop strands requires a self-consistent description for the penetrations and the relaxation process. Here we attempt to study a more general problem rather than a special system like that with permanent penetrations. Numerical methods provide excellent tools for solving such problems. The coarse-grained model mentioned above was studied via a Monte Carlo experiment. The self-diffusion of a primitive chain in a tube was simulated as a stochastic process, and the process of penetration was directly controlled

by the probability p. By employing the Monte Carlo simulation we investigated the process of stress relaxation and the number of penetrations per ring in equilibrium.

It is convenient to think of the curvilinear coordinate for each chain being transformed into a straight, horizontal line so that each chain can be thought of as moving to the *right* or *left* at random. The stress relaxation function $\varphi(t)$ therefore corresponds to the original tube segments remaining at time t [Doi and Edwards, 1986]. The time that the centre of mass of a chain moved a distance l_e, denoted as t_h, was designated as the time step of the Monte Carlo simulation. As a result, given the curvilinear diffusion coefficient $D = k_B T/N_s\zeta$, t_h depended on N since $t_h = \zeta l_e^2 N_s/k_B T$. In the absence of any penetration, the mean relaxation time $\langle\tau_d\rangle$ obtained from the simulation [see Eqs. (4.16) and (4.17) below] appeared to be proportional to N_s^2, one power of N_s being absorbed into t_h.

This Monte Carlo experiment included the effects of chain penetration events as follows. All N_c chains started in the unpenetrated state. At each time step a randomly chosen chain attempted to move rightward or leftward by one unit of length. This move was allowed, and the coordinate of the chain was updated, provided the chain did not contain a passive penetration at the last segment preventing this move; see Figure 4.1. Every chain that successfully moved (i) experienced a corresponding reverse translation of all active and passive penetrations, these being associated with the corresponding tube segments, rather than the chain itself (in our code, as in the physical system, these penetrations remained stationary and only the chain position was updated); (ii) if an active penetration was associated with its trailing tube segment this was annihilated, together with the corresponding passive penetration through a tube segment associated with the other chain; (iii) a new active-passive penetration pair was created with the probability p. In this case the active penetration was associated with the newly created leading tube segment on the moving chain, the corresponding passive penetration was associated with a randomly chosen tube segment on one of the N_c chain. If this segment had had a penetration, either active or passive, or it was the chain leading segment itself, the penetration would be rejected. This scheme tended to lead to an initial increase in the number of penetration pairs (from zero) and a slowing of stress relaxation due to the constraints on the polymer dynamics associated with passive penetrations. Active penetrations themselves did not directly hinder motion.

4.3.3 Execution of the Monte Carlo Simulation

At the beginning of simulation, a single chain was tracked until ten times of tube relaxation had completed. The time steps spent to accomplish this process were

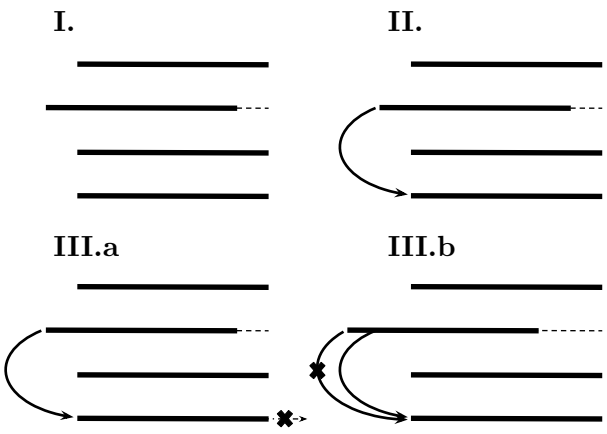

Figure 4.6: A diagram showing how the chain movement and penetration were carried out in the Monte Carlo simulation. **I.** In each time step, a chain was randomly chosen to move along its primitive path, as long as the trailing segment was not blocked by a passive penetration. The direction of movement was also randomly determined. **II.** Once the movement was granted, there was the probability p by which the chain would penetrate a randomly chosen segment from chains, including itself. Here the second chain from the top penetrates the left end of the fourth one by its leading segment (the left end). **III.a** In the next time step, this penetrated chain could not move toward the direction as shown in the figure. This move would be rejected, and the simulation proceeded to the next time step. **III.b** On the other hand, if in the next time step the same chain moved to the left and penetrated the same penetrated segment as that in **II.**, this penetration would be rejected but the movement retained. Notice that the position of penetrations relative to the primitive path do not change with the movement of chains.

averaged to obtain an estimated relaxation time t_e. This was used as a guideline to assess an adequate time interval for the system to reach equilibrium. Based on t_e, the simulation ran for $10t_e$ to let the system reach equilibrium before the formal run, which had $150t_e$. During the formal run, the tube relaxation of all chains were recorded simultaneously until *all* the chains were fully relaxed, and the process was repeated until the maximum time step limit reached. The stress relaxation function $\varphi(t)$ was obtained by monitoring the remaining length of the original tube segments. We calculated the characteristic relaxation time of each chain sample as follows:

$$\tau_j = \frac{\sum_{i=1}^{t_m} t_{ij} t_h \varphi(t_{ij})}{\sum_{i=1}^{t_m} \varphi(t_{ij})}, \tag{4.16}$$

where i was the index of time steps, j the index of chain samples and t_m the maximum time step recorded for the samples. The mean relaxation time over an ensemble of j_s chain samples was then simply computed by

$$\langle \tau_d \rangle = \frac{1}{j_s} \sum_{j=1}^{j_s} \tau_j. \tag{4.17}$$

The number of samples of each simulation run varied because of the stochastic nature of the system, but in general $j_s \sim \mathcal{O}(10^2)$.

4.4 Stress Relaxation of Penetrating Loop Strands

4.4.1 The Slowing of Relaxation Times

In the simulation all the rings were available to penetrate with all the others, i.e. their coil volumes were assumed to be overlapped. The maximum number N_c was therefore limited by the chain number density. The creation of new penetration pairs was rejected if the randomly chosen target segment had been occupied by either an active or passive penetration. According to our mean-field estimation, Eq. (4.19), in the worst scenario the rejection rate would be no more than 1/3 for $p = 0.3$. The actual rejection rate should be lower than this estimation, because the movement of chains was likely blocked first especially when there were a lot of penetrations, while creating new penetrations required such movements in the first place. In other words, the rejection did not directly affect the relaxation time since the creation of penetrations was always executed *after* the chain movement. Figure

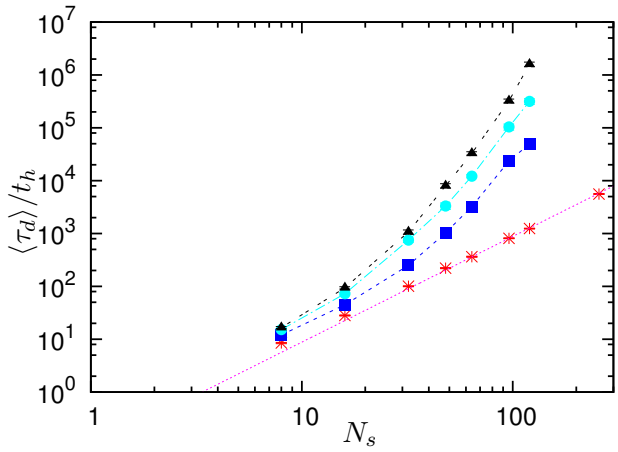

Figure 4.7: Penetrations significantly slowed ring polymer dynamics. The mean stress relaxation time $\langle\tau_d\rangle$ depended on the chain length N_s and the penetration probability p: Shown is data for $p = 0$ (asterisks), 0.1 (squares), 0.2 (circles) and 0.3 (triangles). The Doi-Edwards' scaling $\tau_d^{(0)}/t_h \sim N_s^2$ for linear polymers is shown as a dotted straight line, and the lines connecting the data points are guides to the eye. Error bars are shown but are often invisibly small. The number of chains $N_c = 4$ in these simulations

4.7 shows the variation of mean relaxation time with ring length N_s for various values of the penetration probability p. With a zero penetration probability, the relaxation times followed a power law $\langle\tau_d\rangle \propto N_s^3$, which is what the Doi-Edwards tube model predicts. For the cases of non-zero p, the relaxation time significantly increased with the increasing ring length. When comparing $\langle\tau_d\rangle/t_h$ of the rings having the same length but different values of probability p in Figure 4.7, the differences in magnitude can be as high as the order of 10^4.

Another remarkable finding of the simulation is that the system size, here N_c, strongly controlled the stress relaxation time, shown in Figure 4.8. This is to be expected based on the following simple reasoning. Since the penetration dynamics is always time reversible, there is at least one way to disentangle a system of penetrating rings. While this route may be easily accessible when there are a few rings, when they are numerous (and heavily inter-penetrating) it can be obscure and only slowly accessed by chance.

This effect is more visible in Figure 4.9, which illustrates the penetration events between ring polymers as a directed graph. There are N_c vertices in the graph. Each vertex represents a ring polymer which has a maximum degree equal to the number of segments N_s. The direction of an arrow indicates a penetration event from the penetrating chain towards the penetrated one. Even though one cannot

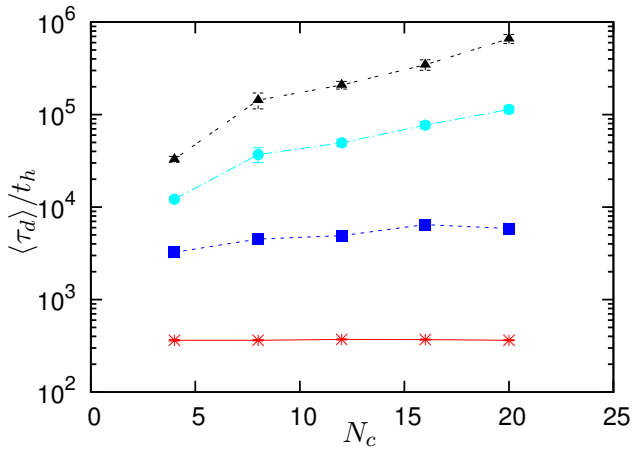

Figure 4.8: The mean stress relaxation time $\langle \tau_d \rangle$ increased with the number of rings N_c available to interpenetrate and on the penetration parameter p: Shown is data for $p = 0$ (asterisks), 0.1 (squares), 0.2 (circles) and 0.3 (triangles). The lines connecting the data points are guides to the eye. Error bars are shown but are often invisibly small. The number of segments $N_s = 64$ in these simulations.

identify a specific order of the relaxation of penetrations from this graph, it is fair to approximate that the longest route of the directed edges takes the longest time to relax. Recall that the penetration events were directly controlled by the penetration probability p, which is exactly the probability to designate an directed edge between a pair of vertices. Therefore our coarse-grained model actually represents a system very similar to that of bond percolation on a random graph. This will be discussed with more details later in Chapter 6.

4.4.2 Penetration Densities

According to Figures 4.8 and 4.9, the number of penetrations per ring m seems to be a key parameter which affects the dynamics of penetrating ring polymers. In the simulation the number of active and passive penetrations was also recorded, and the mean value $\langle m \rangle$, including both active and passive penetrations, in equilibrium was calculated. In the simulation $\langle m \rangle$ appeared to be directly controlled by the probability p, which could be described by the mean-field estimate shown below.

Since in the model a penetration event started (or terminated) from creating (or eliminating) an active penetration, we calculate the time evolution of the active penetrations to understand how the penetration events were controlled via the probability p. The number of active penetrations per ring m_a increased by one whenever the following three conditions were satisfied: (i) a polymer successfully

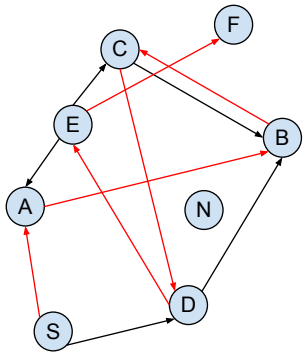

Figure 4.9: A graph representing the relationship of penetrations between ring polymers. A long path of edges can be tracked from S to F via A–E, labelled by red colour. For the ring F, in order to relax it would need all these red edges removed in the reverse way. However, some of the rings lie on the path also are penetrated by other rings. With more ring polymers present and more penetrations linking in such a way, each ring will take a significantly longer time waiting the constraints released.

diffused, which occurred with probability $1 - \langle m_p \rangle / N_s$, where m_p is the number of passive penetrations, (ii) it attempted to create a penetration, which occurred with probability p and (iii) it found somewhere had not been occupied by a penetration to create a new one, which occurred with probability $1 - \langle m \rangle / N_s$. Likewise an active penetration was lost whenever a chain diffused through it, which occurred with probability $\langle m_a \rangle / N_s$. Hence

$$\frac{d\langle m_a \rangle}{dt} = p\left(1 - \frac{\langle m_p \rangle}{N_s}\right)\left(1 - \frac{\langle m \rangle}{N_s}\right) - \frac{\langle m_a \rangle}{N_s} = 0. \tag{4.18}$$

Finally in equilibrium $\langle m_a \rangle = \langle m_p \rangle = \langle m \rangle / 2$ which yields

$$\frac{\langle m \rangle}{N_s} = \frac{3p + 1 - \sqrt{p^2 + 6p + 1}}{2p}, \tag{4.19}$$

which is compared with the simulation data in Figure 4.10.

Although Eq. (4.19) gives a qualitatively correct prediction when compared with the simulation data, the difference between the prediction and the data is easily recognised even for the low p cases. This discrepancy probably originated from the fact that the two types of penetrations did not uniformly distributed along

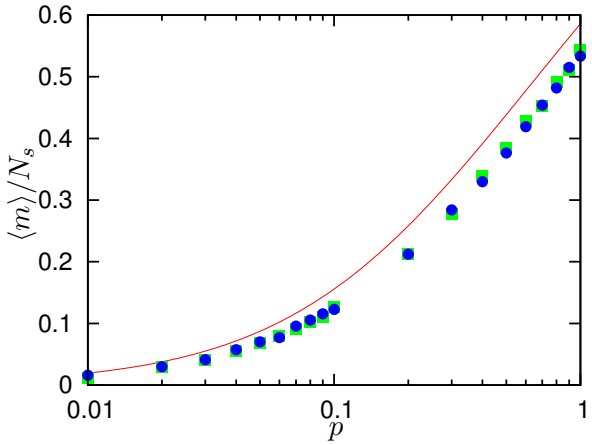

Figure 4.10: Mean number of penetrations per ring normalised by number of segments versus penetration probabilities, for $N_s = 16$ (circles) and 32 (squares). The number of chains $N_c = 4$ in these simulations. The mean-field prediction [solid line, Eq. (4.19)] is qualitatively correct but gives higher values over the whole range of p over which we performed simulations. There is no guarantee that the mean-field argument should be quantitatively accurate, as discussed in the text.

each chain. Despite the *mean* value of m_a and m_p was the same, as expected, the cumulative number of penetrations along the chain showed different distributions between the two penetration types. For example, the two ends of a chain spent more time steps to have active penetrations than the centre of the chain. However, in the case of passive penetrations, the situation was reversed. The non-mean-field *spatial* distribution of penetration might affect the outcome of $\langle m \rangle$ in a way that could not be captured by Eq. (4.18). Nonetheless, for our purposes Eq. (4.19) is an adequate approximation of the simulation data.

While Figure 4.7 shows the variation of relaxation time with ring length N_s for various values of the penetration probability p, it is more informative to plot this against the mean number of penetration per ring $\langle m \rangle$; see Figure 4.11. Explicit N_s dependencies is removed by rescaling the relaxation time by the average time to diffuse a mean-squared distance equal to the average distance between penetrations

$$\tau_e = \frac{[L_c/(m+1)]^2}{\pi^2 D} = \frac{\tau_d^{(0)}}{(m+1)^2}, \tag{4.20}$$

where $\tau_d^{(0)}$ denotes the relaxation time of chains having no penetration, i.e. the disengagement time of the primitive chain in our coarse-grained model.

Here τ_e is called the *encounter time*, and it is a measure of the time interval needed for chain ends to encounter two adjacent penetrations in the original tube;

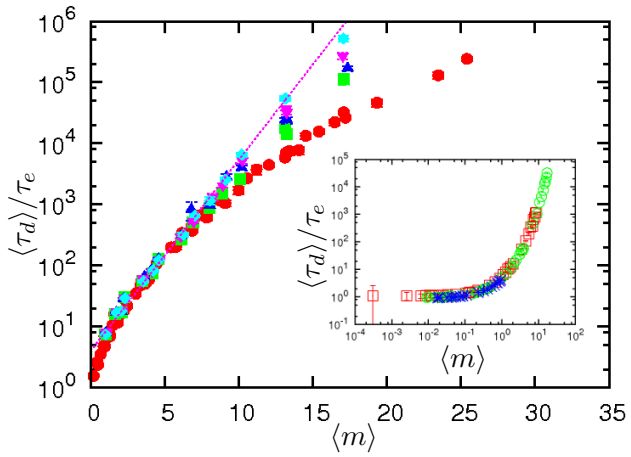

Figure 4.11: The mean stress relaxation time $\langle\tau_d\rangle$, normalised by the encounter time τ_e, increases with the mean number of penetrations $\langle m\rangle$, itself controlled by p, and with the number of rings N_c available to inter-penetrate: Shown is data for $N_c = 4$ (circles), 8 (squares), 12 (triangles), 16 (reversed triangles) and 20 (diamonds). For the largest values of N_c the relaxation is suggestive of an exponential slowing down with the number of penetrations per ring (dotted line). The inset shows the same normalised relaxation time with a very small mean number of penetrations, where $N_c = 4$ with $N_s = 16$ (open circles) and $N_s = 32$ (open squares), and $N_c = 20$ with $N_s = 64$ (asterisks).

see Figure 4.3. Imagine that if, once an end reached a penetration, the penetration had been annihilated immediately, the chain would have relaxed as an ordinary reptation and its relaxation time would have been exactly $\tau_d^{(0)}$. In the real cases, the penetrations often persisted longer than that, hence the chain needed longer to fully relax from the original tube. Therefore, τ_e is a coarse-graining time associated with the fastest physically significant process—the curvilinear diffusion between penetrations (on average). It is the average time which a diffusing chain *tests* the penetration nearest to its ends.

Figure 4.11 shows a dramatic increase of the relaxation time with the increasing number of penetrations, that is consistent with an exponential rise in the largest system ($N_c = 20$). Interestingly, for the simulations of the same N_c, no matter how the other parameters varied, all the obtained $\langle\tau_d\rangle/\tau_e$ fall on the same curve. This suggests that the number of penetration per ring can be seen as a universal parameter of the system. Also, the onset of slowed relaxation is indeed where $\langle m\rangle$ is about the order of unity; see the inset of Figure 4.11. These findings will be discussed with more details later in Chapter 6.

4.4.3 Correction of Correlation Holes and Limited Penetrating Chains

Within the framework of the obstructed reptation, there are several limitations of the Monte Carlo simulation discussed in Section 4.3. To conclude this chapter, we are going to point out the possible consequences of addressing these.

The assumption that a chain is equally likely to penetrate all the chains, including the chain itself, in the Monte Carlo simulation may be questionable. Considering in a body of melt every linear polymer has one monomer labelled, for example, by substituting a hydrogen atom with a deuterium. The structure factor of the melt can be measured via a scattering experiment. If the correlation function, derived from the structure factor, is plotted against the radial distance to a labelled polymer, it will show a sink of signal when the distance is smaller than the radius of the polymer in the melt. This is called the correlation hole [de Gennes, 1979].

The importance of such experiments is that it shows the segment distribution is not uniform in a many-chain system. More precisely, when probing segments around a marked chain in such many-chain systems, it is more likely to find a segment which is part of the marked chain. In the case of entangled ring polymers we expect that there will be also a correlation hole for each ring polymer. The direct consequence of the correlation hole is that, when each loop strand penetrates an arbitrary duplex segment, there is higher probability that this segment belongs to the same loop strand. In other words, in the Monte Carlo simulation, the penetration probability p should have been weighed to favour self-penetration rather than equally likely penetrating all the chains. This effect may be small but becomes significant if the polymer becomes fully compact, where $R_g^3 \sim N_s l_p d^2$.

The second omission is that effectively the simulated system was confined into zero dimensional space. Although the spatial position of ring polymers was irrelevant in the simulation, and as such that there was no real boundary present, the penetrations essentially were *exclusively* created by the N_c rings. In melt of ring polymers, however, even there is a finite number of rings which are fully entangled and penetrated with each other within a volume of space, there should be also penetrations contributed from rings outside of the volume. These rings only partially overlap the observed volume, which contains N_c rings in terms of our simulation. On the other hand, the N_c rings would also partially overlap the neighbouring rings, at the shell region of the observed volume. Some of the active penetrations could create passive penetrations in rings outside of the volume, and the number of passive penetrations inside the volume associated with the N_c chains might reduce accordingly.

Although the total number of penetrations inside the volume may be un-

changed, due to an equal exchange of penetrations at the overlapping region, the dynamics must be affected because the percolating network of penetrations expands to larger extent. The slowing of dynamics shown in our simulation might have been enhanced if the exchange of penetration had been included in the simulation. Nevertheless, the current model is still a good representation of entangled rings when the penetration events are rare, i.e. $\langle m \rangle \sim \mathcal{O}(1)$, because the effect of the penetration exchange would be marginal.

Chapter 5

The Self-diffusion of Entangled Circular DNA

In Chapter 4 we have shown that the penetration between loop strands can strongly slow down the stress relaxation. It is obviously of interest to find experimental evidence of such a dynamic behaviour in entangled ring polymers. We used circular DNA as the ring polymer to carry out a simple experiment to study its self-diffusion in a concentrated solution. One advantage of using DNA is that it is relatively easy to produce unknotted circular DNA with a very narrow distribution of molecular weights. By exploiting this advantage it is possible to observe the dynamics of entangled ring polymers without many contaminants. In this experiment, we used fluorescence microscopy to observe a trace of labelled DNA molecules and track their positions. In such a way, the dynamics of the entangled circular DNA can be studied by analysing the mean-squared displacements.

5.1 Circular DNA as a Ring Polymer

5.1.1 Circular DNA

We chose a plasmid DNA called pUC19 to be the ring polymer in this experiment. pUC19 is one of the most widely used cloning vectors in molecular biology. It is a circular double-stranded DNA (dsDNA) and has 2,686 base pairs (bp). The reason behind this choice was that pUC19 was readily available, being produced on a massive scale in the laboratory. We used DH5α *E. coli* cells (New England BioLabs Inc.) to replicate pUC19 through transformation. After the transformation, these *E. coli* cells were able to form colonies on LB (lysogeny broth) agar plate against the antibiotic ampicillin. The cells taken from the colonies then were further grown

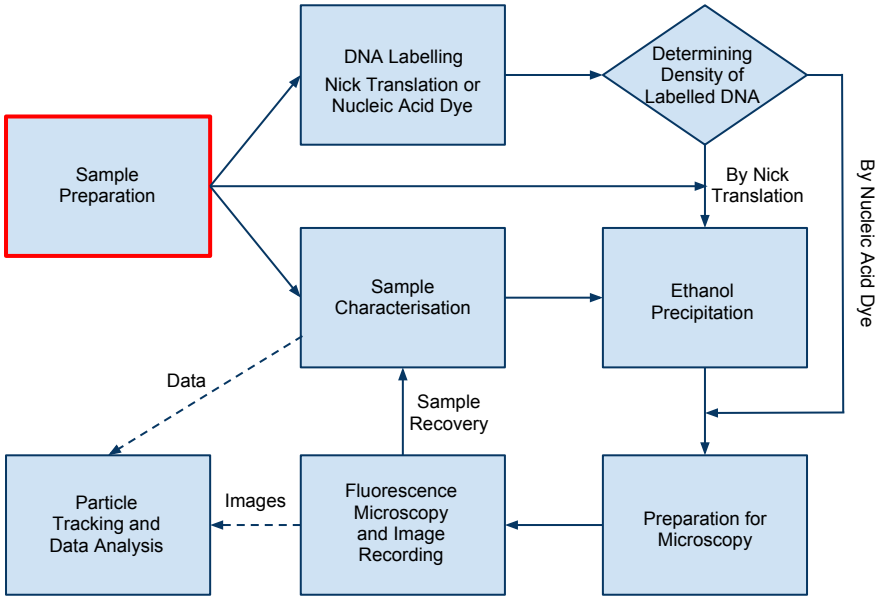

Figure 5.1: A flow chart representing the experimental protocol.

in LB with ampicillin. The grown *E. coli* cells in the LB were finally processed using the QIAGEN Plasmid Mega Kit to isolate and purify the plasmid DNA from the bacteria.

It has been well known for decades that circular dsDNA has two different conformations. The slight unwinding found in supercoiled plasmid DNA cause the helical axis to twist about itself such that it resembles a linear rod. Supercoiled DNA is converted to open-circular (OC) DNA by the introduction of a single breakage in one of the two strands (a nick). The nick provides the degree of freedom for the chain to relax such tension by rotating the strand, hence the DNA can maintain its circular conformation in a solution. Therefore, studying the topological constraints emerged from the penetration between ring polymers would require to keep pUC19 in its open-circular conformation. In the experiment we used the nicking endonuclease Nt.BspQI to introduce a single nick on one strand of pUC19.

Figure 5.2 shows an agarose gel in which pUC19 samples processed by enzymes feature various lengths and conformations. The linear chromosomal DNA ($>$ 10 kbp, not shown in the gel) was removed by exonuclease III (ExoIII). ExoIII could be also active at nicks and make an open circle become a circular single-stranded DNA (ssDNA), which should have higher mobility than the supercoiled

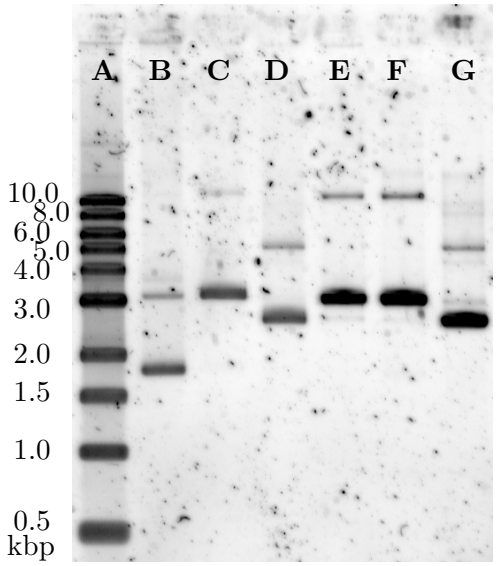

Figure 5.2: An 1.2% (w/w) agarose gel which features various pUC19 samples and 1 kbp ladder (Lane **A**). Lane **B**, **C** and **D** are the control pUC19 which present the supercoiled, open-circular and linear conformation, respectively. The samples nicked by Nt.BspQI are shown in Lane **E** and **F**. The lane at the right end is of the sample of linear pUC19.

DNA. However, the gel did not show the existence of such DNA in the samples. The non-existence of circular ssDNA has been confirmed by adding Nt.BspQI to nick the DNA after the reaction of ExoIII. Presumably the circular ssDNA, if any, would remain as Nt.BspQI only acted on duplex DNA. In Figure 5.2 it is clear that no stained DNA can be found beyond the open-circular pUC19 at Lane **E** and **F**. This suggests that no circular ssDNA had presented in the sample. We also prepared linear pUC19 to compare the dynamics with the open-circular DNA in the later analysis. These linear pUC19 molecules were made by cutting the circular pUC19 with the restriction endonuclease HindIII at the corresponding site. In Figure 5.2 it is shown in Lane **G** that the front band falls at the position between 2.0 and 3.0 kbp, as expected.

When a plasmid is maintained in *E. coli*, two copies of the plasmid will become joined covalently by homologous recombination to form a dimer, identical to the monomer except that it contains two copies of the plasmid in a single circle with twice the contour length of the monomer. It is impossible to remove the unwanted dimeric pUC19 by just adding enzymes to target on it specifically, because the enzymes would be active on the monomeric pUC19 as well. Nonetheless, the dimeric pUC19 only comprised a small fraction of the whole sample. In Figure 5.3

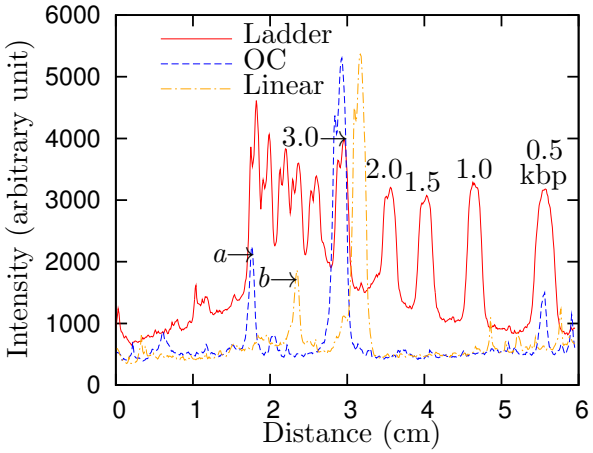

Figure 5.3: The profile of the fluorescence intensity of the stained DNA shown in Figure 5.2. The front of loading wells of the gel is designated as the origin of the distance. Here only the profiles of Lane **A** (ladder), **F** (open-circular pUC19) and **G** (linear pUC19) are displayed. The peaks indicated by a and b are the dimeric open-circular pUC19 and dimeric linear pUC19, respectively.

the dimeric pUC19 is indicated by a and b for the sample of open-circular and linear pUC19, respectively.

There were two methods available to us to label the DNA. One is called the nick translation; DNA polymerase I (Pol I) was used to replace some of the nucleotides starting from nicks with their labelled analogues, in this case, Cy3-dCTP (GE Healthcare). When Pol I detached from the DNA, it left a nicked site some base pairs away from the original one. The DNA was first nicked by Nt.BspQI, then the nicking enzyme was deactivated by heat. Later dATP, dGTP, dTTP, Cy3-dCTP and Pol I were added into the solution. The mixture was incubated overnight and then purified consecutively by phenol-chloroform extraction and QIAquick PCR Purification Kit (QIAGEN). After the labelling, most of the pUC19 molecules had one nick and were tagged by each nicked site with a Cy3 fluorophore.

The other method was to use a nucleic acid dye to stain the DNA directly. In this research we chose to use a dimeric cyanine nucleic acid stain called YOYO-1 (Molecular Probes, Invitrogen; 1,271 daltons). It has not only a high affinity for nucleic acids but also a very high fluorescence quantum yield which results in very bright fluorescence signals. We diluted the stock YOYO-1 solution by 1,000-fold to 1 μM using Tris-EDTA (TE, 10 mM Tris-HCl and 1 mM EDTA) buffer and mixed the solution with the DNA samples ($\approx$ 100 ng/μL) by a volume ratio of 4:1. Before mixing the labelled DNA molecules with the unlabelled, concentrated ones, the labelled DNA molecules were centrifuged through Micro Bio-Spin 30 columns

(Bio-Rad) in order to remove the free flowing YOYO-1 in the solution to prevent them staining the unlabelled DNA afterwards. The column selectively removed small molecules (< 40,000 daltons or 20 bp nucleic acids) from the DNA solution. This method has been proved effective, because the density of labelled DNA did not change after mixing the labelled and unlabelled DNA molecules.

At the early stage of this work, the preferred labelling method had been the nick translation using the fluorophore-coupled nucleotide Cy3-dCTP. This labelled the pUC19, either linear or open-circular, in a well controlled manner, and the bonding of fluorophore to the DNA was robust because of the covalent bonding of the phosphate backbone. Unfortunately, an issue regarding the conformation of the circular pUC19 put the suitability of this method in doubt. The gel electrophoresis of the samples taken from various steps of nick translation showed that the labelled pUC19, which was supposed to have at least one nick, had a higher mobility similar to the supercoiled pUC19 only after purification. At this moment we cannot specify whether it is that its conformation changed from the open circle to the supercoil or there was any profound effect of the labelling upon the mobility in gel electrophoresis. As a consequence, we chose to use YOYO-1 to label the pUC19 instead. As shown in Figure 5.4 (**b**), the gel showed that the mobility of pUC19 only slightly changed after the labelling. This is expected since the changes of the dsDNA persistence length in a good solvent by dimeric cyanine nucleic acid dyes has been well characterised in the literature [Bakajin et al., 1998; Doyle et al., 2000]. Hence both the open-circular and the linear pUC19 were thought to remain the conformations after the labelling. In this work only the same conformation of the DNA molecules, both labelled and unlabelled ones, were mixed together to be observed on the microscope. This allowed us to follow dilute *tracer* molecules in a background of unlabelled chains.

5.1.2 Preparation of Concentrated Solutions

Here we define a concentrated solution of DNA by the concentration being higher than ten times of its overlap concentration $C^{\star}$, acknowledging that this regime is not clearly defined in the context of polymer physics [de Gennes, 1979; Doi and Edwards, 1986]. In order to reach such high concentrations, it is most convenient to extract DNA by ethanol precipitation and resuspend the precipitated DNA with a small volume of TE buffer.

Ethanol precipitation is a widely used technique in molecular biology to purify or concentrate DNA [Sambrook et al., 1989]. The highly charged phosphate backbone of DNA can be stabilised by water molecules, which form hydration shells

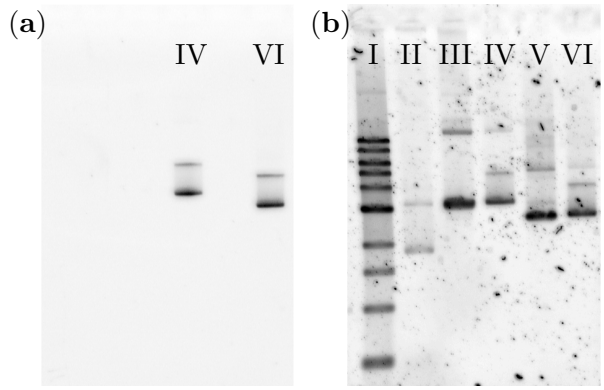

Figure 5.4: (**a**) The gel before stained by SYBR Gold. At the moment only the YOYO-1 labelled DNA showed fluorescence. (**b**) The gel showed all the lanes after stained by SYBR Gold. In Lane I it showed the same 1 kbp ladder as that in Figure 5.2, Lane II the supercoiled and open-circular pUC19, Lane III and IV the open-circular pUC19, and finally, Lane V and VI the linear pUC19. The mobility of both open-circular and linear pUC19 after labelling was slightly slower than the original ones.

around these negative charges. On the other hand, adding ethanol to solution reduces the effectiveness of charge screening from the hydration shells. With the presence of positive charges, electrical attraction between the phosphate groups and these counterions can be strong enough to form ionic bonds and hence collapse the DNA so that it can be precipitated.

In this experiment each volume of unlabelled DNA (10–35 ng/μL) was mixed with 0.1 volume of 3 M sodium acetate (pH 5.3) and two volumes of ice-cold absolute ethanol. After being on ice for 15–30 minutes, the ethanol solution was centrifuged with a high speed ($\approx$ 20,000×g) at 0°C for 10 minutes. Because the volume of the microcentrifuge tube is limited to 1.5 mL, and there was normally 10–15 mL of the ethanol solution to be centrifuged, we needed to separate the solution and centrifuge it repeatedly in the same tube to collect all the precipitated DNA as a single, large pellet. Afterwards the pellet was washed by 70% ethanol and centrifuged again with the same high speed at 4°C for 2 minutes. Later the supernatant liquid was removed, and the microcentrifuge tube was dried at room temperature until the last traces of fluid had evaporated. Finally the pellet was resuspended by 4 μL of TE buffer [Sambrook et al., 1989]. Then the pellet dissolved in the buffer for overnight, and thereafter 1 μL of the labelled DNA was added into the solution. Contrary to the normally practised routine, we did not add the oxygen scavenger[1], used to reduce

[1]The final concentration of the constituents would be as follows: 4.5 mg/mL glucose, 0.2 mg/mL glucose oxidase, 0.035 mg/mL catalase and 0.5% (w/w) β-mercaptoethanol.

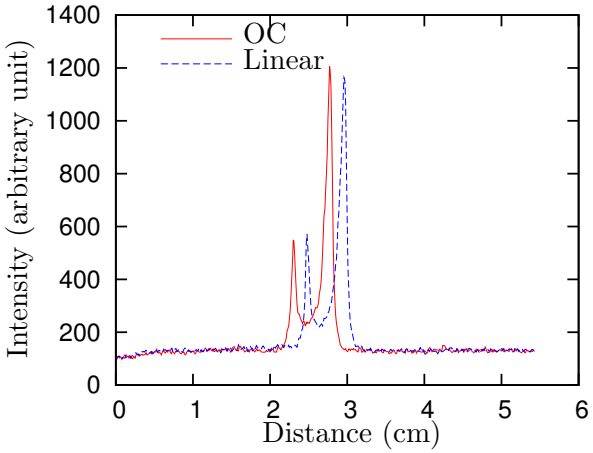

Figure 5.5: The profile of the fluorescence intensity of the YOYO-1 stained DNA in the gel shown in FIG. 5.4 (**a**). The front of loading wells of the gel is designated as the origin of the distance. The conformation of the DNA corresponding to the second, smaller peak of each profile is unclear. It might be the fluorescence from the dimeric pUC19. However, in both samples, these molecules migrated faster than the dimeric pUC19. See Figure 5.4 (**b**) Lane III–VI.

photobleaching due to the intense light beam of a fluorescence microscope, into the buffer. The presence of any protein (e.g. glucose oxidase in the oxygen scavenger) in the sample would have affected the absorption of ultraviolet light when using the spectrophotometer to quantify the DNA concentration later. Therefore the samples were kept as purified dsDNA as much as possible in order to obtain accurate readings from the spectrophotometer.

5.2 Fluorescence Microscopy

5.2.1 Preparation for Observation

As the self-diffusion of the labelled DNA is of greatest interests in this experiment, all the factors which affected the motion of DNA and the later tracking had to be eliminated [Crocker and Hoffman, 2007]. The microscope had been fitted on an optical table, which was lifted by air to stabilise it from vibration transmitted through the floor and walls. Each sample was sealed in the small chamber using Gene Frame (Thermo Scientific) on a standard thin glass cover slip (thickness 0.12–0.17 mm); see Figure A.1. Gene Frame is a commercial product designed to isolate reaction on a glass cover slip from external environments. Between the polystyrene cover slip of Gene Frame above and the glass cover slip below the sample, there

were two layers of Parafilm (Pechiney Plastic Packaging Company) to sustain the aqueous solution by its waxy, hydrophobic surface. The sample was injected by a laboratory pipette at the centre of the bottom Parafilm, where there was a hole of 5.5 mm in diameter. The glass cover slip was treated by a plasma cleaner beforehand and the surface exposed through the hole of the Parafilm was coated by 6 mg/mL BSA (bovine serum albumin) and later washed by deionised water. The cleaning and coating prevented most of the DNA from adsorbing on the glass surface.

5.2.2 Observation and Particle Tracking

The samples were observed using an Olympus IX71 inverted fluorescence microscope and Andor iXon EMCCD (electron-multiplying CCD) camera. The image was magnified by an 100× oil objective (NA 1.4) and an 1.6× integrated magnifier within the microscope. The physical size of the images taken by the camera was 51.07×51.20 μm, provided a resolution of 512×512 pixels.

Despite the control panel of iXon EMCCD camera is capable of changing exposure time to under 33.3 ms, the recording frame rate is fixed at 30 frames per second (FPS). In fact we found that the resulting average frame rate with the exposure time set at 33.3 ms was 28–29 FPS, probably due to a lag of transmitting and writing the raw images to the hard disc drive.

When starting the observation, we first tuned the focus to find the surface of glass cover slip by searching for fixed fluorescent spots, which were mostly DNA adhered on the surface. These fluorescent spots sometimes were autofluorescent particles, but they usually had very different sizes and shapes from the DNA so that it was easy to distinguish them from each other. After locating these spots, at which the focus was supposed to be close to the glass surface, we rotated the fine tuning knob to move the focus upwards to a position 25 μm above the surface.

The images were taken from several regions in each sample. One of the important criteria of choosing such regions was to avoid any slow, large fluorescent particles that were unlikely to be DNA. The other important factor was the brightness of the labelled DNA as the photobleaching limited the duration of observation within the volume exposed to the excitation light beam. The exposure time was always set at 33.3 ms, and there were 2,100 consecutive frames taken from each region. The restriction of taking only 2,100 frames was posed by the file format requiring huge amount of memory for analysis, and the accessible memory on our computer used to perform particle tracking was just barely able to handle these. On average, the time span of the images for each region was about 70 seconds.

In this work the particle tracking was accomplished by using an IDL (Inter-

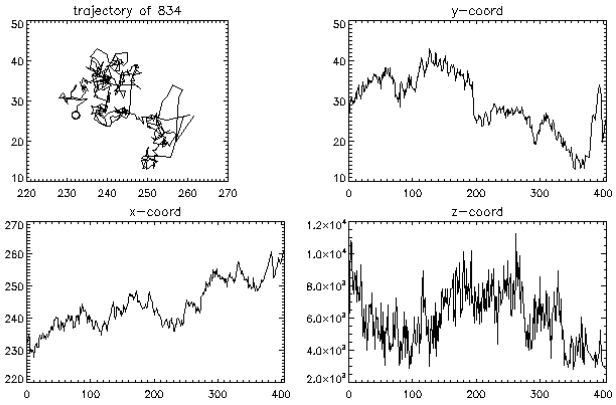

Figure 5.6: An example of the trajectory and the time evolution of positions in x-, y- and z-coordinate of a tracked DNA molecule. The positions in z-coordinate shown in the figure are actually the intensity fluctuation of fluorescent signals. In this work we only performed two-dimensional tracking, which only required the positions in x- and y-coordinate.

active Data Language) package[2] developed by John C. Crocker and David G. Grier; Eric R. Weeks also has contributed a few supplemental routines. This package is capable of identifying multiple particles in each frame, according to given parameters for filtering and centroid locating, and linking their positions between frames to establish trajectories of the particles [Crocker and Hoffman, 2007].

5.2.3 Quantification of the DNA

The DNA samples were recovered from the sealed chamber on the cover slips to quantify their concentrations. 2 μL of each sample was recovered by a 0.1–10 μL pipette tip and put into a 0.5 mL microcentrifuge tube. The samples were then diluted by 25-fold with TE buffer.

The concentration of DNA can be determined by its absorption of ultraviolet light at 260 nm using a spectrophotometer. This is based on Beer-Lambert law by which, regarding nucleic acids, an optical density (OD) of unity corresponds to a concentration of 50 ng/μL for dsDNA [Sambrook et al., 1989]. However, instead of using a standard cuvette, which would have a 10 mm optical path length, we used a special cuvette designed for small volumes of sample to perform the measurement. In accordance to the 1 mm path length of this cuvette, an OD of 0.1 now corresponds to a concentration of 50 ng/μL for dsDNA.

Table 5.1 lists the average readings of absorption measurements following the

[2]This package can be downloaded at http://www.physics.emory.edu/∼weeks/idl/.

Sample	A_{260}	$\delta_{A_{260}}$	A_{280}	B_{320}	Ratio	δ_{ratio}
L_1	0.2331	0.0001	0.1313	0.0024	1.7902	0.0014
L_2	0.2348	0.0001	0.1329	0.0042	1.7910	0.0010
L_3	0.2403	0.0001	0.1378	0.0080	1.7908	0.0018
OC_1	0.4143	0.0001	0.2314	0.0027	1.7997	0.0019
OC_2	0.4145	0.0002	0.2312	0.0025	1.8015	0.0013
OC_3	0.4428	0.0005	0.2529	0.0113	1.7858	0.0007

Table 5.1: Absorption of ultraviolet light in the unit of OD. A_{260}, A_{280} and B_{320} is the absorption of the sample at 260, 280 and 320 nm, respectively. B_{320} serves as the background test such that it is denoted by B. The ratio is calculated as follows: (A_{260}-B_{320})/(A_{280}-B_{320}). The notation L stands for linear and OC for open-circular. Each sample was repeatedly measured for five times. The values shown in this table are the average over the five measurements for each sample. $\delta_{A_{260}}$ and δ_{ratio} is the standard error of A_{260} and the ratio, respectively.

procedures described above. Converting the readings of OD to concentrations and taking average over the three samples from each conformation, we obtain the mean concentration of both samples. The concentration of the open-circular pUC19 is 5.3 μg/μL and that of the linear pUC19 is 3.0 μg/μL. Notice that the ratios listed in Table 5.1 are all very close to 1.8. These suggest that the samples are pure DNA without contamination such as proteins [Sambrook et al., 1989].

5.3 The Self-diffusion of Entangled DNA Molecules

5.3.1 Mean-squared Displacements

The mean-squared displacement is the ensemble average of squared displacements over a number of particles travelling in a given time interval, the lag time τ_l, and can be written as

$$\langle \Delta x_j^2(\tau_l) \rangle = \langle [x_j(t+\tau_l) - x_j(t)]^2 \rangle, \tag{5.1}$$

where x_j is the particle position and j the coordinate index [Crocker and Hoffman, 2007]. The particle tracking package links positions of each particle located in consecutive frames to form the trajectory for the particle according to given parameters.

The most important parameter of tracking is the maximum distance of movement between frames. This value has to be set somewhat smaller than the average distance between particles, otherwise the programme would mistakenly recognise multiple particles as a single one. This particular issue mostly arises from the fact that these particles also randomly move along the vertical directions. Several particles close to each other could appear and disappear between frames so that the

programme would link these particles, which contribute to larger displacements in the later stage of analysis.

The other two parameters are used to deal with the false identification of noise and the temporary disappearance of particles, at which they moves away from the focus. In our analysis, any trajectory sustained less than 10 frames, namely, ≈ 330 ms, was discarded for that it was likely from the noise. Particles temporarily disappeared for at most 3 frames, ≈ 100 ms, were still considered to be the original particles instead of new ones.

The package not just calculates the mean-squared displacements but also the mean displacements, which is supposed to be zero for an ideal Brownian particle in isotropic matrix. In experiments, however, it is more likely to observe horizontal drifting in many cases. Even though we had taken precautions against such a drifting, for instance, to maintain the temperature of the stage and the objective at 22°C, to fix the cover slip on the stage tightly and so on, there was still a slow drifting detected. The package does compensate such drifting by computing $\langle \Delta x_j^2(\tau_l) \rangle - \langle \Delta x_j(\tau_l) \rangle^2$. This is the final values used as the mean-squared displacement, and the two-dimensional mean-squared displacements,

$$\langle \Delta r^2(\tau_l) \rangle = \sum_{j=1,2} \langle \Delta x_j^2(\tau_l) \rangle - \langle \Delta x_j(\tau_l) \rangle^2, \tag{5.2}$$

are shown in Figure 5.7. Notice that the number of particle samples of each lag time would be inversely proportional to τ_l, but the actual decline of the sample number is worse than that since the particles eventually moved away from the focus. In order to obtain statistically significant results, we only take the mean-squared displacements which have more than 1,000 samples as valid results. Consequently, the range of τ_l shown in Figure 5.7 is far less than the true time span of the videos.

5.3.2 The Comparison of Relaxation Times

We use the function $f(\tau_l) = a\tau_l^b$, where a and b are the fitting parameters, to fit the mean-squared displacement versus the lag time τ_l. The results are as follows. The mean-squared displacement of the linear pUC19 is fitted by $a = 1.2486 \pm 0.0042$ and $b = 0.9553 \pm 0.0048$. The mean-squared displacement of the open-circular pUC19 is fitted by $a = 0.8756 \pm 0.0145$ and $b = 0.7938 \pm 0.0117$. Then we consider various time scales and try to understand the dynamics behind the results of mean-squared displacements as follows.

The radius of gyration R_g of λ-DNA (48,502 bp) was reported to be 0.73 μm in good solvents [Smith et al., 1996]. By assuming a Kuhn length to be 300 bp

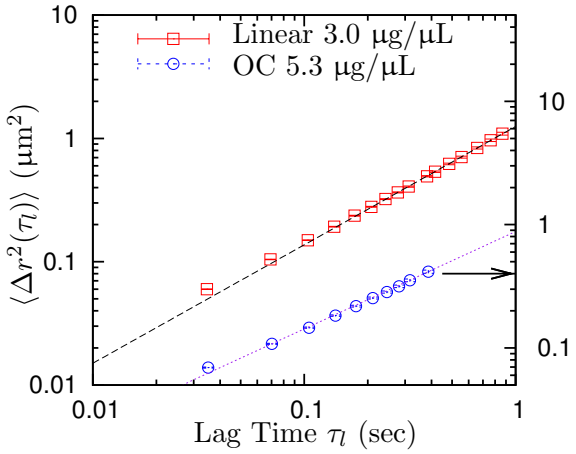

Figure 5.7: The two-dimensional mean-squared displacements of the linear and open-circular pUC19. The linear pUC19 demonstrates a typical self-diffusion behaviour which is linearly proportional to the lag time. However, the open-circular pUC19 follows a power law which has an anomalous exponent 0.8. The fitting lines are also shown in this figure: $\langle \Delta r^2(\tau_l) \rangle = 1.25 \times \tau_l^{0.96}$ (black dashed line) and $\langle \Delta r^2(\tau_l) \rangle = 0.88 \times \tau_l^{0.79}$ (purple dotted line).

[Marko and Siggia, 1995a] and the Flory exponent to be 0.588 [Cotton, 1980], we can estimate R_g of pUC19. For a linear pUC19 in good solvents, its R_g is estimated to be 0.133 μm. Hence the overlap concentration $C^\star$ of the linear pUC19 can be easily calculated and it is 0.3 μg/μL. For an open-circular pUC19, by adopting the result derived by Zimm and Stockmayer [1949], its R_g is estimated to be 0.089 μm and the overlap concentration is 1.0 μg/μL.

The Rouse time of both the linear and open-circular pUC19 could be well below the shortest lag time available in our analysis, which is limited by the fixed frame rate of videos. The Rouse time is

$$\tau_R = \frac{4\zeta N R_g^2}{3\pi^2 k_B T}, \tag{5.3}$$

where the friction constant $\zeta = 12\pi\eta_s R_g$ and η_s is the viscosity of the solvent [Doi and Edwards, 1986]. Here we consider the temperature to be 20 or 25°C, thus the corresponding viscosity of the solvent, assuming water, is 1.002×10^{-3} or 8.9×10^{-4} Pa·s, respectively. Therefore the Rouse time of the linear pUC19 is 26.55 ms at 20°C and 23.19 ms at 25°C. The Rouse time of the open-circular pUC19 is 7.96 ms at 20°C and 6.95 ms at 25°C.

The disengagement time $\tau_d^{(0)}$, on the other hand, is difficult to accurately assess since we lack information on the entanglement length. The entanglement

length serves as a parameter in the Doi-Edwards tube model and it is critical for estimating the dynamics of entangled linear polymers. For the ring polymer, it is unclear in what conditions the tube model is still relevant as a good approximation. Nevertheless, according to the estimation of $C^\star$ and τ_R above, we expect to see that these pUC19 molecules fully relax and demonstrate a standard diffusion behaviour for any lag time longer than 100 ms.

In Figure 5.7 it is clear to see that both linear and open-circular pUC19 follow a power law, $\langle \Delta r^2(\tau_l) \rangle \propto \tau_l^b$, but only the linear pUC19 shows a standard diffusion behaviour in which $b \approx 1.0$ according to the fitting above. For the open-circular pUC19, despite not being highly entangled, its mean-squared displacement follows a power law with $b \approx 0.8$. The origin of this anomalous power law is unclear at the moment.

Finally, a remark regarding the difference of the dynamics between the linear and the open-circular pUC19 should be made here. It has been reported that concentrated ring polymers move faster than their linear counterparts at the same concentration [Robertson and Smith, 2007; Kapnistos et al., 2008]. This is understandable in the dilute limit since the ring polymer has a smaller R_g than its linear counterpart. As for the concentrated solutions, these groups of authors concluded that ring polymers did not entangle with each other as well as linear polymers. Therefore, the confinement on each ring polymer from the neighbouring chains was not as effective as that in linear polymers.

Here our experimental data might support this point of view. Despite the linear pUC19 had a lower concentration (but reached $10C^\star$) than the open-circular pUC19, both samples had similar magnitudes of the mean-squared displacement over the range of lag times shown in Figure 5.7. The fact that the concentration of the open-circular pUC19 did not reach $10C^\star$ indicates that its degree of entanglements might not be as high as the linear pUC19 in the experiment. The experimental results will be discussed with more details in Chapter 6.

Chapter 6

Ring Polymers as Topological Glass

So far we have demonstrated the theoretical calculation, the Monte Carlo simulation and the experimental data of entangled ring polymers. In this chapter we will proceed to discuss the meaning of these results obtained from Chapter 3–5. We will show how our results can be linked to future studies, for example, to experimental data of viscoelasticity of entangled ring polymers. More importantly, we will illustrate the implication of existence of topological glass according to these results. In the last section some topics for future studies are briefly introduced. We believe these topics will eventually help us better understand entangled ring polymers and the topological glass.

6.1 Penetration Densities and Universality

In Chapters 3 and 4 we already discussed a simple model of entangled ring polymers, which allowed the rings to penetrate each other. We then further developed the model to a coarse-grained model based on the assumption that the penetration events only occurred in a perturbative sense. Therefore, we built the model in which the ring polymer was treated as if it was a linear chain with additional constraints other than just the confinement of surrounding chains.

One of the most important conclusions we draw from the simulation is that the mean number of penetrations per ring fundamentally controls the dynamics. It is shown in Figure 4.11 that $\langle m \rangle$ represents a universal parameter of the entangled ring polymers. According to Figure 4.11, therefore, one may write down a

phenomenological equation

$$\langle \tau_d \rangle = \frac{\tau_d^{(0)}}{(\langle m \rangle + 1)^2} e^{C_0 \langle m \rangle}, \tag{6.1}$$

where C_0 is a constant only depending on N_c and $\langle m \rangle$ following Eq. (4.19). The exponential term can be expressed as a Taylor series such that

$$\langle \tau_d \rangle = \frac{\tau_d^{(0)}}{(\langle m \rangle + 1)^2} \left(1 + C_0 \langle m \rangle + \frac{C_0^2 \langle m \rangle^2}{2} + \cdots \right). \tag{6.2}$$

For the cases in which there are only a few penetrations among the polymers, that is, $\langle m \rangle \ll 1$, one can approximate $\langle \tau_d \rangle$ as

$$\langle \tau_d \rangle \approx \tau_d^{(0)} \left(1 + \frac{C_0 \langle m \rangle}{2\langle m \rangle + 1} \right) = \tau_d^{(0)} + \Delta\tau_d. \tag{6.3}$$

Once C_0 and $\langle m \rangle$ are determined, one can use Eq. (6.3) to estimate the relaxation time of entangled ring polymers if the penetration events are rare. Unfortunately, there are two problems that have to be dealt with. Firstly we currently do not have sufficient simulation data to determine the form of C_0. The only thing we know is that the normalised relaxation time $\langle \tau_d \rangle / \tau_e$ follows the same curve if N_c is fixed, thus C_0 must depend on N_c; see Figure 4.11. Even if we could relate N_c to the chain density and the radius of gyration, it is still unclear how C_0 could be expressed in terms of N_c. The second problem is that $\langle m \rangle$ is determined by N_s and p, where the probability p is an artificial parameter controlling the stochastic dynamics in the simulation. Before we can estimate $\langle m \rangle$, the microscopic origin of p in the entangled ring polymers should be better understood.

Nevertheless, Eq. (6.3) has an implication of great importance regarding the viscoelasticity of entangled ring polymers. Since the steady state viscosity can be obtained through the exact integral

$$\eta = \int_0^\infty G(t) dt, \tag{6.4}$$

where $G(t)$ is the relaxation modulus, it is also true that $\eta \approx G\tau_d$ with G being an effective modulus [McLeish, 2002b]. Eq. (6.3) shows that a correction to the steady state viscosity should be measured in the entangled ring polymers if there are penetrations.

In real systems the situation is probably not as simple as that predicted

by Eq. (6.3), as our model is a mean-field model based on several simplifications. Moreover, we have assumed that each ring polymer behaves like a linear object, and the fluctuation of the ring polymer along this linear path (the primitive path) eventually makes it diffuse and relax from the original position. This is in contrast to the picture in which the rings tend to segregate, according to some of the computer simulations mentioned in Chapter 2. As yet there is no experimental evidence to verify our model for now, this prediction requires further investigation to confirm its validity.

An interesting remark about Eq. (6.2) is that it is very similar to the virial expansion for the pressure of many-particle system in equilibrium. This might be just a coincidence, because the exponential function was chosen to fit the data, and the Taylor expansion of an exponential function is also a power series. The reasons behind why our simulation data have such a trend deserves detailed investigation in the future. Nonetheless, a simple interpretation can be made as follows. In our model of loop strands, the fundamental relaxation mode is reptation. Without any penetration the relaxation is the same as the Doi-Edwards prediction. As long as there are penetrations, these penetrations *interact* with each other through the topological constraints and change the relaxation time. The effect of such *interactions* between penetrations becomes stronger when there are more penetrations between rings. Here one can treat the number of penetrations per ring m as the counterpart of the particle density ρ in the virial expansion. As a result, one may further express the relaxation time of penetrating loop strands as follows:

$$\frac{\tau_d}{\tau_d^{(0)}} = 1 + C_1 m + C_2 m^2 + C_3 m^3 + \cdots, \tag{6.5}$$

where C_i, $i = 1, 2, 3, \cdots$, are the dimensionless coefficients corresponding to the virial coefficients in the virial expansion. At this moment, unfortunately, there is no analytic calculation which gives these coefficients.

6.2 Implications of Simulation and Experimental Data

6.2.1 Temperature Dependence of Viscosity

By comparing Figures 4.7 and 4.11, one may want to generalise the expression of Eq. (6.1) in terms of more accessible variables. Since $\langle m \rangle$ can be determined by N_s and p, see Eq. (4.19), one can use the parameters N_s and λ, a function characterising the extent of penetrations, to express the relaxation time. As a result, the steady

state viscosity of entangled ring polymers becomes

$$\eta(T) \approx G\tau_d = \eta_0(T)e^{\lambda(T)N_s}, \tag{6.6}$$

where G is an effective relaxation modulus and $\eta_0(T) = G\tau_0(T)$ the viscosity before penetrations taking effect. The relaxation time τ_0 appears to depend on temperature explicitly since $\tau_0 \sim \zeta N_s R_g^2/k_BT$. However, for ring polymers in solutions $\zeta \sim k_BT/6\pi\eta_s l_p$, and $R_g \sim N_s^\nu l_p$, thus both quantities depend on temperature as well. The persistence length is inversely proportional to temperature, as $l_p = E_y I/k_BT$, where E_y is the Young's modulus and $I = \pi d^4/64$ [Doi and Edwards, 1986]. Although the temperature dependency of η_s can be in forms of exponential functions, for example, in the Arrhenius model, but this dependency is irrelevant in our consideration. We are interested in the effect of the topological constraints in this study, and the ring polymers have been assumed capable of relaxing through thermal fluctuation. Therefore, the relevant temperature is likely of the order 10^0–10^2 °C, and η_s can show a weak temperature dependency at such temperatures, like the viscosity of water near room temperatures. Comparing these quantities, we conclude that τ_0 may be inversely proportional to temperature under the conditions relevant to our model.

The parameter λ is probably a function of density ρ, the number of segments per unit volume. In our simulations, ρ did not explicitly appear in the coarse-grained model. Instead we used the penetration probability p to determine the extent of penetrations. The penetration probability p can be crudely estimated by the volume fraction of N_c chains occupying a space $V \sim R_g^3$, where $N_c \sim \rho R_g^3/N_s$, and thus

$$p \sim \frac{N_s l_e d^2 N_c}{V} \sim \frac{N_s l_e d^2 \rho R_g^3/N_s}{R_g^3} = \rho l_e d^2. \tag{6.7}$$

Moreover, λ should also reflect the fact that, with more rings occupying the volume V, the penetrations will significantly prolong the relaxation process. This corresponds to the growth rate of $\langle\tau_d\rangle/\tau_e$ that varies with different values of N_c shown in Figure 4.11. It is unclear what the temperature dependency of λ looks like, but λ is certainly a function of p and N_c. From the discussion above, λ essentially is a function of persistence length and so it must depends on temperature. The key is the mathematical form of λ, in particular, the prefactor may be important to determine how it should vary with temperature.

Compared with the Vogel-Fulcher law of typical glass formers [Binder and

Kob, 2011],

$$\eta(T) = \eta_0 \exp\left(\frac{B}{T - T_0}\right), \tag{6.8}$$

Eq. (6.6) also shows an exponential growth in viscosity but can be dependent on temperature in a different fashion. The Vogel-Fulcher law does not have robust theoretical foundation, but it gives a good representation of the experiment data. Likewise, Eq. (6.6) may represent a special type of the glass transition which has a different origin of the frozen molecular motion. Indeed this resonates with our idea that the entangled ring polymers form a disordered material with slow dynamics simply due to the topological constraints. More importantly, our Monte Carlo code solved a well posed problem, the curvilinear diffusion in inter-penetrating rings, which could be extended to lattice trees. Thus it represents a potentially tractable universal class of glass formers, indifferent of, for instance, chemical compositions of the rings. In this sense Eq. (6.6) is considered universal for the topological glass.

6.2.2 Time Dependence of Mean-squared Displacements

At the end of Chapter 5 we compared the experimental data with the Rouse times. It turned out that the time scales of observation were likely longer than the disengagement times of these entangled DNA molecules, thus a standard diffusion behaviour was expected for both topologies of DNA. It is puzzling, however, that the circular DNA showed a sublinear time dependence in its mean-squared displacements, $\langle \Delta r^2(\tau_l) \rangle \propto \tau_l^{0.79 \pm 0.01}$. Milner and Newhall [2010] reported the mean-squared displacement of centrality, considered as the counterpart of centre of mass in their model of lattice trees, scaled with time as $\langle \Delta c^2 \rangle \sim t^b$ where $b = 0.75$–0.8. However, this may be just a coincidence that this result agrees with our observation. We need to stress that this reported result was based on the scenario in which a lattice tree diffused between an array of fixed obstacles. This is the limit in which the ring must *compactify* to the conformation of a lattice tree. Such a regime is only expected when the concentration or the molecular weight of ring polymers is sufficiently high.

We already showed in Chapter 5 that the concentration of the circular pUC19 was only about five times of its overlap concentration. Therefore we are sceptical that the sample was sufficiently entangled to show properties similar to that in permanent confinement of gel fibres. Furthermore, in a recent molecular dynamics simulation reported by Rosa et al. [2011], the authors showed that the mean-squared displacements of unknotted rings followed the standard linear time dependence when above the squared radius of gyration. In our experimental data, the smallest mean-squared displacement is beyond the squared radius of gyration, hence the data should

demonstrate a linear time dependence as well.

One possible explanation of the anomalous exponent is that it is an artefact of the particle tracking. According to our experience of performing the fluorescence microscopy experiment, many sources can introduce errors into the tracking of labelled DNA. The tracking is done via automatic image processing and centroid locating, thus inevitably the quality of images greatly affects the outcome. Although we had taken a lot of effort to eliminate several possible error sources, the tracking might not be as accurate as we expected and possibly led to some systematic error.

More importantly, our data show that the conditions of the experiment were far from where we would have hoped to achieve. As explained in Chapter 2 and 3, the significantly slower stress relaxation of penetrating rings is detectable only when the ring polymers are highly entangled. It is obvious that our samples were just barely entangled such that the relaxation time was hardly affected by penetrations between rings. One critical factor which made the experiment fail to reach the necessary entangled state was that the circular DNA we used was too short. The contour length of pUC19 is only about nine times of its Kuhn length in good solvents. In order to create sufficient entanglements for each ring, the concentration of the DNA would have needed to be very high, but we only managed to concentrate the circular DNA to a concentration even less than $10C^{\star}$. Without a plasmid up to tens of kilo base pairs, it was impossible to test either our speculation of the topological glass or the properties of ring polymers in gels at a concentration which was reasonably achievable in a standard biochemical laboratory.

6.3 Some Topics for Future Studies

6.3.1 Improved Simulation Methods

As it was indicated in Chapter 4, a main advantage of our coarse-grained model is that it guarantees the loop strands are sufficiently long compared with the entanglement length without overwhelming the computation power. We estimate that the performance of our code scales with the size of simulated system as $\mathcal{O}(N_s N_c)$. This advantage have been proved beneficial by the simulation data because the mean relaxation time scaled with N_s exponentially. If we had simulated the system down to monomeric scale, the computation time would have been roughly N_e times longer, where N_e is the number of monomers between entanglements. On the other hand, such a coarse-grained model ignores mesoscopic structure and dynamics, which could also be important to the phenomena we are interested in. In particular the diffusive motion of these loop strands is assumed a priori without rigorous mathematical

derivation.

An alternative approach is to employ highly detailed simulations, either Monte Carlo simulations or molecular dynamics simulations, to study the ring polymers. Many researchers have done such simulations for years, but they are too slow for the dynamics that interests us. With the progression of computation hardware in the past decade, now we have more and more computation power at our disposal at a reasonable price. The development of parallel computation, especially the introduction of general-purpose computing on graphics processing units (GPGPU), is attracting a lot of attention among the community of scientific computation. Nonetheless, for simulating dynamics of the glass transition, one may need more sophisticated algorithms than parallel computation.

In the past few decades a majority of research of the glass transition was done by using computer simulations. It was mainly because the strongly slowing dynamics of the glass transition made experiments very difficult to proceed. However, this is also a problem for computer simulations, especially for the molecular dynamics simulations due to the extremely broad time scales involved in the simulations. Certain levels of simplification to release the computation burden is still necessary when using most of the readily available machines in the nowadays marketplace, which are already several orders more powerful than the machines in the 1980s. In any case, a revision of the simulation model is likely to be fruitful when parallel computation is implemented into the algorithm in the future. A dynamic coarse-graining algorithm may be helpful to manage computation resources in a more efficient way. We wish the new detailed simulation will also benefit us to investigate the validity of the model of lattice trees described in Chapter 3.

6.3.2 Penetrations as a Network of Percolation

In Chapter 4 it was briefly mentioned that the process of penetrations between rings could be seen as a problem of directed graph. Here we are going to explore this idea a bit more. We have discussed the similarity between the penetration of ring polymers and the percolation model on a directed graph. Typically the percolation model on random graphs is limited to the graphs with Poisson degree distribution at their vertices [Callaway et al., 2000]. This is one of the major differences between our model and the random graph, as the degree of each vertex in our model is bound to the segment number N_s. Nonetheless, when the penetrations are rare, this penetration graph should approximate to the percolation model on a random graph.

From a different point of view, one can also treat the entangled ring polymers

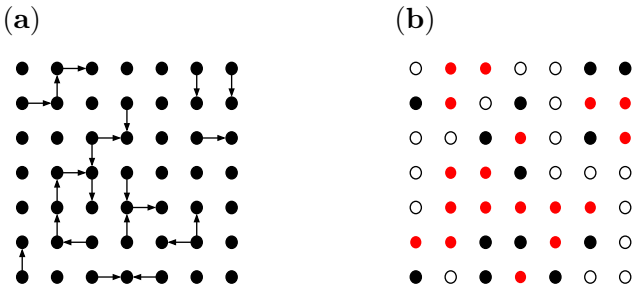

Figure 6.1: (**a**) An example of bond percolation which represents the penetrations in a melt of ring polymers. (**b**) The bond percolation shown in (**a**) can be mapped to a spin system according to the corresponding dynamic behaviours of each site. There are rings without penetration (open circles), rings with exclusive active penetrations (black closed circles) and rings with passive penetrations (red closed circles).

as a bond percolation problem on lattices instead of graphs. This is detached from our model based on the tube model since there is no *tube* introduced to the scheme below, although it is still true that each ring is thought as a lattice tree. The purpose of this new scheme is not to calculate the measurable quantities quantitatively but merely to illustrate how penetrations affect the dynamics. Let us consider a hypercubic lattice with a dimensionality δ. On each site there is a particle presenting a ring polymer. The bonds of the lattice represent the segments of each ring polymers, namely, N_s. Thus for rings with N_s segments, the lattice has to have a dimensionality $\delta = N_s/2$.

The simplest situation in the scheme is that there is no penetration between polymers. Hence the lattice can present melt of linear or branched polymers. Such a model can be employed in Monte Carlo simulations. Given a probability to exchange a pair of nearest-neighbouring polymers, it can simulate the relaxation process of the melt. Once all the possible configuration changes have been made, in which the time correlation of the sites becomes zero, one may see the system as being fully relaxed. The relaxation time is supposed to be the total time steps normalised by the size of the simulated system.

One can also randomly add bonds between nearest-neighbouring sites to represent penetrations of ring polymers; see Figure 6.1 (**a**). Every bond is designated with a specific direction, which is from the penetrating ring towards the penetrated

one. At this stage one already has a bond percolation problem in hand, although it is a slightly more complicated one since the bonds are directed. In any case, what really complicates the situation is the consequence of adding these bonds. As we have discussed in Chapter 4, the relaxation of ring polymers is directly restricted by passive penetrations. In such a percolating system, the penetrating rings are still able to move and to exchange the site with other available rings. On the contrary, any penetrated ring is pinned down at its own site until its passive penetrations are all removed.

In a classic percolation system, either it is site percolation or bond percolation, there is a probability threshold P_∞ which determines the transition point above which all the sites are linked as an infinite cluster. It is proved that P_∞ is related to dimensionality of the lattice. From the previous computer simulations it is shown that the threshold P_∞ decreases with the increasing dimensionality [Stauffer and Aharony, 1992]. Similar to these classic percolation systems, one also expects that the configuration of the lattice system mentioned above shows an infinite cluster at an arbitrary time if the penetration probability p' (denoted differently from p used in simulations for clarification) is larger than a certain threshold.

The real challenge of analytic calculations for this model, however, will be the dynamic process of exchanging rings according to the type of penetrations. Only the pure sources of the directed bonds and the bond-free sites are able to move freely. When there are a lot of penetrations between the rings, it is more likely that most of the sites are constrained by some others. Intuitively, a bigger cluster takes longer time to fully shuffle its configuration, namely, the time correlation function of the sites within the cluster does not vanish even a long time has passed. Although this seems to be a very different model from that discussed in Chapter 4, one may be able to obtain analytic results of C_0 and Eq. (6.1) from studying this percolation model.

6.3.3 Connections to Spin Glass

The percolation model described above can be expanded to a related field of disordered solids. In a ferromagnet the random dilution of spins with competing ferro- and antiferromagnetic interactions leads to a frustrated state [Binder and Kob, 2011]. At a temperature T_f a freezing transition occurs, and such ferromagnets are called the *spin glass*. If on one particular observation a spin is $\vec{S}_i^{(1)}$ then if it is observed again a long time later, there is a nonvanishing probability that $\vec{S}_i^{(2)}$ will point in the same direction [Edwards and Anderson, 1975]. In other words, the time correlation of the spin will be $\langle \vec{S}_i^{(1)} \cdot \vec{S}_i^{(2)} \rangle \neq 0$. The Hamiltonian of such a spin

system can be written as

$$\mathcal{H} = -\sum_{i \neq j} J_{ij}(\vec{S}_i \cdot \vec{S}_j) - H \sum_i S_i^z. \tag{6.9}$$

The lattice sites are labelled by i (and also j when necessary). Each site carries a n-component spin $\vec{S}_i$ of length $|\vec{S}_i| = 1$. J_{ij} is the exchange interaction energy and H the strength of magnetic field. This is a general expression of the n-vector model [Chaikin and Lubensky, 2000], but actually a Potts model with $q = 3$, i.e., each spin having three states available, is sufficient to describe the percolation of penetration network.

In our percolation model there will be three different states of each site and two types of dynamic behaviour. Each site can be occupied by a bond-free ring, an active-penetration-exclusive (APE) ring or a penetrated (PP) ring. Only the first two are able to exchange its site with nearest-neighbouring sites, if they are available. Hence one may model the lattice as each site having a spin with a value of 1, 0 or -1 to present its state; see Figure 6.1 (**b**). By intuition one can imagine that there should be configurations in which a great number of APE rings are unable to find sites to exchange their positions. As a result, these *spins* are trapped in the frustrated states and the configuration is frozen.

Although the idea is very simple, the challenges come from how one can write down the proper exchange interaction energy J_{ij} for such a percolation system. It is obvious that the exchange energy between sites of different states should vary according to the combination of the pairs. For example, exchange between a bond-free ring and a PP ring is forbidden since the PP ring is trapped by penetrations. In the theoretical model of spin glasses, the randomness of the system is determined by J_{ij} via a probability distribution $P(J_{ij})$. If following the same approach, then a more complicated $P(J_{ij})$ has to be used instead of the simple Gaussian distribution which gives $P(J_{ij}) = P(-J_{ij})$ [Binder and Kob, 2011]. An even trickier issue is how the bonds linked between APE and PP rings are modified once APE rings change sites. At this moment it is unclear how one can progress with this spin model, but the resemblance between it and the percolation model should not be ignored easily.

Chapter 7

Conclusions

The goals of this work were to build a theoretical model for studying the dynamic properties of unknotted ring polymers at high densities, and to measure such properties experimentally. The topological constraints emerging from the circular topology could lead to a glassy state in which the process of stress relaxation became extremely long. Ultimately we were looking for evidence of such glass transition.

The development of the theoretical model began from adopting the ansatz that the conformation of entangled ring polymers resembled a lattice tree. Our mean-field model incorporated with the argument based on a recurrence relation describing the branching structure of lattice trees. This model was further simplified into a coarse-grained model representing the entangled ring polymers as loop strands, and the simplified model was employed in the Monte Carlo simulation. We also attempted to produce ring polymers with a narrow distribution of molecular weights. The circular DNA pUC19 was replicated via bacterium transformation in a massive scale. The DNA was processed by proper enzymes to ensure its conformation remained a trivial circle. The dynamics of the DNA was studied by observing a trace of labelled DNA in the concentrated DNA solution via fluorescence microscopy.

The major results and findings of this research are as follows. With the argument of structural recurrence, the grand canonical partition functions of a lattice tree were easy to calculate. The volume fraction of ring polymers of which the mean-field model is to hold falls in the range $N_s^{1/4}(d/l_p)^2 \ll \phi \lesssim 1$. Each ring polymer—as a lattice tree—can be viewed as a linear object with an end-to-end distance of the backbone section as

$$R_b \gtrsim \left(\frac{d}{l_p}\right)^{2/3} N_s^{1/3} l_p. \tag{7.1}$$

These results have provided the basis of the coarse-grained model employed in the Monte Carlo simulation and the experimental conditions for using the circular DNA

as the ring polymer.

The Monte Carlo simulation showed that the relaxation time increased exponentially with the increasing length of ring polymers. The relaxation time also increased with the increasing number of rings. The number of rings, which corresponded to the actual system size in the simulation, was associated with a reversible percolating network formed by the penetrations between rings. More importantly, the number of penetrations per ring m was identified as a universal parameter which related to the relaxation time as follows:

$$\tau_d = \frac{\tau_d^{(0)}}{[m(p, N_s) + 1]^2} \exp[C_0(N_c)m(p, N_s)]. \tag{7.2}$$

This relation suggested that the viscosity of penetrating loop strands could be written in the form $\eta(T) = \eta_0(T) \exp[\lambda(T)N_s]$. The viscosity grew exponentially with the increasing penetrations, and it might have a different temperature dependency from the common glass transition. The simulated system essentially represents a potentially tractable class of glass formers.

As for the experiment, the translational movement of the concentrated linear and circular DNA was tracked through the particle tracking technique. The circular DNA showed a sublinear time dependence in its mean-squared displacements, $\langle \Delta r^2(\tau_l) \rangle \propto \tau_l^{0.79 \pm 0.01}$. This result was unexpected since the range of mean-squared displacements was above the squared radius of gyration; a linear time dependence should have been shown in the data instead. Unfortunately, the experimental data were not enough to clarify the origin of this anomalous behaviour. Although the experiment turned out to be inconclusive, this was mostly due to the limitations of the experimental conditions rather than conclusive evidence that such topological glass is not present.

In spite of the inconclusive result, our experimental method has shown its potential for studying the dynamics of entangled ring polymers. The length and conformation of DNA can be easily controlled by using appropriate enzymes. There are also many techniques to manipulate or label DNA for specific purposes or conditions. The particle tracking technique used in this work is capable of tracking a great number of particles automatically, therefore it can save a lot of time and achieve higher quality of results.

Furthermore, the theoretical models and simulation suggest that the topological glass may be found in entangled ring polymers. Although it only included penetrating loop strands, the model employed in the simulation can be extended to include lattice trees. Treating each entangled ring polymer as a phantom lattice

tree established a reasonable description of such a system. Equilibrium properties, such as the average size of rings, can be calculated with the topological constraints improvised into the mathematical expression. Therefore, our models and simulation have demonstrated that studying the entangled ring polymers qualitatively is well achievable.

The work described in this thesis is just a beginning of studying the dynamics of entangled ring polymers and the topological glass. Several topics for future studies have been discussed in Chapter 6. Other than improving the simulation and considering related analytic models of the glass transition, the following research directions may also enhance the understanding of such systems.

The Monte Carlo simulation has provided the information of dynamics of the penetrating loop strands. The coarse-grained model can be extended to penetrating lattice trees based on this information. This can be done by considering each lattice tree as a combination of multiple loop strands and slipping knots at branching points. The new model can be employed in the Monte Carlo simulation with only minor changes in the current programme code.

The grand canonical partition functions of lattice trees led to the equilibrium properties in the calculation, but the cases of exerting steady forces on both sides of the backbone section was overlooked in this thesis. A detailed calculation for such conditions may be helpful to the understanding of how entangled ring polymers response to the topological constraints. Its predictions also can be used to be compared with experiments using optical tweezers to stretch a confined ring polymer in the future.

Finally, we still believe that the topological glass may be physically accessible in experiments, as our simulation analysis has shown in this thesis. The circular DNA should have been far beyond entangled states if very long DNA at the same concentration had been used in the experiment. Using very long plasmid DNA (> 50 kbp), an entangled state can be reached at a concentration of the order of 100 ng/μL. We estimate that the corresponding DNA concentration of the regime considered in our model will be at the order of 10 μg/μL. Preparing DNA solutions in a volume of 10 μL at such concentrations is manageable in a standard biochemical laboratory. Hopefully experimental evidence of the existence of topological glass, for example, in concentrated plasmid DNA solutions, can be found in the future.

Appendix A

Protocols and Procedures of the Experiment

A.1 Sample Preparation

- The λ-DNA (48,502 bp) for testing purposes is a commercial product manufactured and sold by Fermentas. The stock concentration is 0.3 μg/μL and the weight of the DNA for each aliquot is 500 μg.
- The circular DNA pUC19 (2,686 bp) is produced from DH5α *E. coli* cells (New England Biolabs Inc.) via transformation. The source pUC19 is a commercial product manufactured and sold by New England Biolabs Inc. The protocol of transformation and growing the *E. coli* is as follows.

  a. First thaw a tube of DH5α *E. coli* cells on ice for 10 minutes.

  b. Add 0.5 μL DNA solution containing 0.5 ng pUC19 for each 5 μL of the *E. coli* cells. Prepare three aliquots, and add pUC19 into two aliquots and one without it. Carefully flick the tube 4–5 times to mix cells and pUC19. **Do not vortex the tube**.

  c. Place the aliquots on ice for 30 minutes. **Do not vortex the tube.**

  d. Heat shock the aliquots at exactly 42°C for exactly 30 seconds. **Do not vortex the tube**.

  e. Place the aliquots on ice for 5 minutes. **Do not vortex the tube**.

  f. Dilute the aliquots containing pUC19 100- and 200-fold, respectively, in LB. Dilute the aliquot without pUC19 100-fold in LB.

  g. Spread 25 μL of the diluted cells from each aliquot on a LB agar plate containing ampicillin, respectively. Incubate overnight at 37°C.

h. Inspect the colonies grown on the LB agar plates. Note that the cells without pUC19 should not be capable of forming any colony on LB agar plate against ampicillin. Follow the instruction of QIAGEN Plasmid Mega Kit to grow the *E. coli* in LB. After spinning in LB for an appropriate time, isolate and purify the pUC19 from the bacteria in LB using the kit.

- The oxygen scavenger is prepared as follows. Each 100 volumes contain (1) glucose (150 mg/mL) 3 volumes, (2) glucose oxidase (20 mg/mL) 1 volume, (3) catalase (3.5 mg/mL) 1 volume, (4) β-mercaptoethanol (50%, $\sim$ 7.15 M) 1 volume and (5) TE buffer 94 volumes.

A.2 Sample Characterisation

- Concentration Measurement Using Spectrophotometer

  a. Dilute the sample down to a concentration less than 500 ng/μL.

  b. Turn on the desktop PC and start the RNA/DNA software module of spectrophotometer. Tick the option **background check** and set the wavelength to be 320 nm.

  c. Transfer 5 μL of 1× TE buffer on the cuvette lens (specifically designed for tiny drop volumes) of the spectrophotometer to perform blank measurement. Clean the lens and transfer 5 μL of each sample on the cuvette lens. Start the measurement and repeat the procedure until all samples has been measured. Clean the lens when finished.

  d. Notice that this cuvette has a shorter optical path length thus the reading requires a correction factor 10 to match the normal cuvette; that is, now the reading 0.1 represent a concentration 50 ng/μL for dsDNA.

  e. The ratio A_{260}/A_{280}, or $(A_{260} - B_{320})/(A_{280} - B_{320})$ if background check performed, of a pure DNA sample should be 1.8.

- Gel Electrophoresis Using Agarose Gel

  a. Weigh 0.7 g agarose powder on a balance for each 100 g solution (for preparing 0.7% agarose gel).

  b. Dissolve the agarose with 1× TAE (Tris-acetate-EDTA, 40mM Tris, 20mM acetic acid and 1mM EDTA, pH 8.0) buffer in a beaker until the whole solution reaches the wanted concentration.

  c. Heat the solution using a microwave oven until it is nearly boiled.

d. Cool the whole beaker by water flow until hands can hold the beaker.

e. Pour the solution into a gel mould with the well mould in place. Wait for 30–60 minutes.

f. Remove the well mould and put the gel mould with the gel altogether in an electrophoresis tank. Pour 1× TAE buffer into the tank until the whole gel is covered by the buffer.

g. Prepare samples to run the gel electrophoresis. For each five volumes of sample, add one volume of loading dye and mix. Note that the concentration of DNA sample is recommended to be lower than 10 ng/μL, or the volume of sample injected to each well should not be more than 20 μL, to prevent saturation of fluorescent signal during scanning later.

h. Carefully inject each sample (loading dye added) into the wells by pipette. Connect two electrodes to the power supply. Be aware of the relative position of the wells and the two electrodes. Set the voltage to 75 V (or a voltage giving an electric field 7.5 V/cm) and run the electrophoresis for one hour.

i. Turn off the power supply and remove the gel from the mould. Prepare 50 μL of 1× TAE buffer with 10 μL SYBR Gold (nucleic acids dye) stock solution added in. Gently stir the buffer until the dye is uniformly mixed. Soak the gel into the buffer and wait for 15–20 minutes. Put the gel on a ultraviolet light table or scanner to see the result.

A.3 Nick Translation

1. First of all the DNA to be labelled has to be nicked. For every 250 μL reaction it contains 25 μL 10× NEB (NE Buffer) 2, 10 μg of DNA and deionised water. *Optional:* Remove a 25 μL aliquot for agarose gel test later. Then add 2 μL of 10 unit/μL Nt.BspQI into the solution. Incubate the aliquot at 50°C for 2 hours. Deactivate the nicking enzyme at 80°C for 20 minutes. *Optional:* Remove a second 25 μL aliquot for agarose gel test later.

2. Now the DNA is labelled via nick translation. Firstly add 2.5 μL of 2 mM dATP, dTTP and dGTP into the reaction, respectively. Then add 5 μL of Cy3-dCTP stock solution into the reaction. Finally add 10 μL of DNA polymerase I into the reaction. Incubate the aliquot at 25°C overnight. *Optional:* After the reaction, remove a third 25 μL aliquot for agarose gel test later.

3. Extract the DNA once with equal volume of phenol and once with chloroform from the aqueous phase after a short centrifuge in a tabletop centrifuge. Most of the dye and the enzymes end up in the non-aqueous phase.

4. Purify the DNA from free nucleotides remaining in the solution by using QIAquick PCR Purification Kit (split reaction into two) or gel filtration with Micro Bio-Spin 30 columns (split reaction into three). Alternatively, it can also be purified via ethanol precipitation especially when very long DNA (> 10 kbp) is labelled. Remove the final 25 μL aliquot for agarose gel test.

5. Prepare 0.7% agarose gel with TAE buffer and perform gel electrophoresis with 75 V for one hour to confirm the success of labelling.

A.4 Extraction Using Ethanol Precipitation

1. Prepare the DNA sample whose concentration is between 10–30 ng/μL. Mix one volume of the DNA sample with 0.1 volume of 3 M sodium acetate (pH 5.3).

2. *Optional:* Add 1–10 μL of the Cy3 labelled DNA sample into the mixture if it is to be observed. Be aware that YOYO-1 labelled DNA is very likely to lose the affinity of these fluorophores after the precipitation.

3. Add two volume of ice cold absolute ethanol into the tube and mix by vortex. Put the tube on ice for 15–30 minutes.

4. Transfer the ethanol solution into a *single* 1.5 mL microcentrifuge tube and centrifuge the solution with a high speed ($\geq 15,000\times$g) at 0–4°C for 10 minutes. Remove the supernatant fluid carefully and be aware not to let pipette tip contact the pellet or the tube wall above it. Repeat this process using the same microcentrifuge tube until all the ethanol solution has been centrifuged.

5. Fill the tube half way with 70% ethanol solution and centrifuge the sample with the same high speed at 4°C for 2 minutes. Remove the supernatant carefully as the last step. Put the tube on bench at room temperature or on a dry bath heater at 45°C until the last traces of fluid have evaporated.

6. Dissolve the DNA pellet with deionised water or TE buffer. Note that up to 50% of the DNA is smeared on the wall of the tube (mostly above the pellet). To recover all of the DNA, it is necessary to work a drop of fluid on the tip backward and forward over the appropriate quadrant of wall. For more

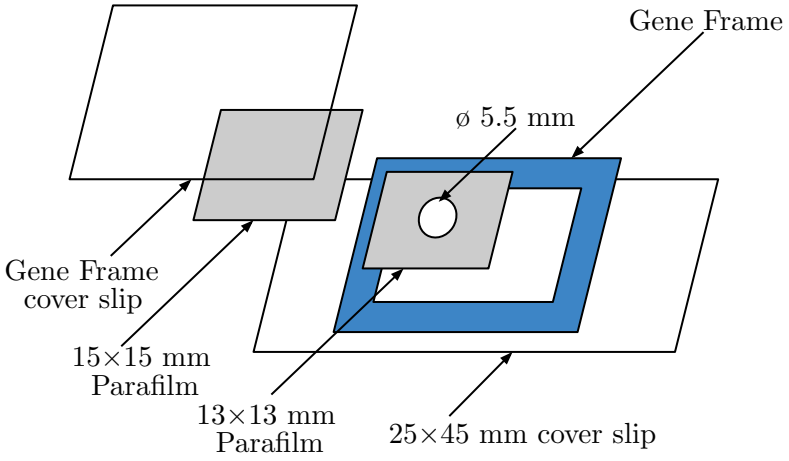

Figure A.1: Instruction diagram of the cover slip with Gene Frame.

detailed information of the protocol please refer to the book of Sambrook et al. [1989].

A.5 Preparation for Microscopy

1. Process 25×45 mm glass cover slips (thickness 0.12–0.17 mm) in a plasma cleaner for 15 minutes. Cut Parafilm into 13×13 and 15×15 mm squares. Punch a hole (diameter ≈ 5.5 mm) at the centre of each 13×13 mm Parafilm using a typical paper puncher. Notice that in order to have a clean edge of the holes, you will have to punch the Parafilm with several layers of paper.

2. Put a 13×13 mm Parafilm at the centre of a 25×45 mm processed cover slip. Put a 15×15 mm Parafilm on a polystyrene cover slip of Gene Frame and press the Parafilm with a curved object to ensure that it tightly fits on the surface. Gently heat the 25×45 mm cover slips on a lens tissue via dry bath heater at 55°C for 30 minutes, then press the Parafilm with your fingers carefully to make it tightly fit on the surface.

3. Take a Gene Frame and follow the manual to put off the plastic sheet of Gene

Frame. Carefully place the Gene Frame on the 25×45 mm cover slip. Now it should surround the 13×13 mm Parafilm. Press the edge of Gene Frame through the plastic sheet still covering the other side to ensure the Gene Frame tightly fit on the glass surface. Now put off the remaining plastic sheet. Notice that the surface of Gene Frame is very sticky so be careful not to touch or let any object contact it.

4. Inject 5 μL BSA solution (6 mg/mL) inside the hole of the 13×13 mm Parafilm and rinse it with deionised water after 5 minutes. Let the surface dry and then transfer 5 μL of sample solution inside the hole of the 13×13 mm Parafilm.

5. Slowly cover the Gene Frame using the polystyrene cover slip with the 15×15 mm Parafilm facing the 13×13 mm Parafilm. Be aware that if the sample is very aqueous, the sample will easily flow through a gap between the two Parafilm layers. Use a finger to press the edge of the Gene Frame to make it air tight sealed.

6. Store the whole cover slip in a box at 4°C.

A.6 Fluorescence Microscopy (Using Olympus IX71)

1. Turn on the desktop PC and mercury lamp burner. Also turn on both the stage and objective temperature controlling devices (including the cooler pump). Open aperture to let the light pass through the objective. Start the control panel of Andor iXon EMCCD camera and wait 20–30 minutes for the camera cooling down to −70°C and the temperature of stage and objective reaching the wanted range.

2. Apply some immersion oil to the 100× oil objective (NA 1.4). Remember that the magnifier under the filter cube rotor has to be pulled out (1.6×) if the software has been calibrated according to this set up. Place the sealed sample above the objective on the stage and fix its position tightly. Raise the objective until the immersion oil slightly contact the cover slip and squash.

3. Rotate the filter cube rotor to WIG for Cy3 or the other proper cube set, depending on the fluorescent dye used on the sample. Choose a saved profile or change the camera setting manually, e.g., EM gain, pre-gain, exposure time, etc., then click *Live* button to observe the microscopic image.

4. Rotate the coarse tuning knob to find some static bright spots, where the focus is possibly near the surface of the glass contacting the sample solution.

Use the fine tuning knob to raise the objective by 25 μm (25 clicks, counter-clockwise). Fix at the position of the objective and only move the stage to search for suitable regions for observation and recording.

A.7 Recording Images

1. Search for a region in which there are around 100 visible labelled DNA molecules.
2. Determine a proper frame interval by observing the random motion of the labelled DNA. For more details please refer to the paper of Crocker and Hoffman [2007]. Choose an appropriate exposure time and number of averaging frames according to the quality of image.
3. If the frame interval required is longer than 30 seconds, record the images by taking snapshots and control the aperture manually to protect the labelled DNA from photobleaching. Use a timer to count the interval as accurate as possible.
4. If the fame interval required is shorter than 30 seconds, set a suitable exposure time and frame averaging number and record videos while exciting the labelled DNA continuously. Due to the large size of saved file, it is not recommended to exceed 2,100 frames fro each recording.
5. Save the images or videos in TIFF format (default 14-bit TIFF) and copy the files to an external USB hard disc drive. Leave saved files on the desktop PC as backup for future recovery.

A.8 Particle Tracking Using IDL

The particle tracking kit for IDL, created by John C. Crocker and David Grier, was used to track the labelled DNA in the recorded images of fluorescence microscopy. To read the tutorial please visit http://www.physics.emory.edu/∼weeks/idl/. For more detailed discussions of the error sources please refer to the paper of Crocker and Hoffman [2007]. Note that the default save format of the iXon camera is 14-bit TIFF. In order to read the file correctly in IDL using *readtiffstack.pro*, the main array to store the pixel data has to be declared by **LONARR** instead of the original **BYTARR** (line 22 and 23). In *epretrack.pro*, line 106, the option */lomem* should be deleted. This is (probably) a legacy option used when the user wants to save memory. But when run on CSC (The University of Warwick) Linux desktop an

syntax error would be shown and terminate the routine. The deletion of this option prevent the routine from termination and does not affect the execution. For more details of the programmes in this package please refer to the comments in the source code.

Bibliography

G. Adam and J. H. Gibbs. On the temperature dependence of cooperative relaxation properties in glass-forming liquids. *The Journal of Chemical Physics*, 43(1):139–146, 1965.

C. A. Angell. Formation of glasses from liquids and biopolymers. *Science*, 267(5206): 1924–1935, 1995.

V. Arrighi, S. Gagliardi, A. C. Dagger, J. A. Semlyen, J. S. Higgins, and M. J. Shenton. Conformation of cyclics and linear chain polymers in bulk by SANS. *Macromolecules*, 37(21):8057–8065, 2004.

O. B. Bakajin, T. A. J. Duke, C. F. Chou, S. S. Chan, R. H. Austin, and E. C. Cox. Electrohydrodynamic stretching of DNA in confined environments. *Physical Review Letters*, 80(12):2737–2740, 1998.

L. Berthier and G. Biroli. Theoretical perspective on the glass transition and amorphous materials. *Reviews of Modern Physics*, 83(2):587–645, 2011.

K. Binder and W. Kob. *Glassy Materials and Disordered Solids*. World Scientific Publishing Company, Incorporated, 2011.

M. Bohn and D. W. Heermann. Topological interactions between ring polymers: Implications for chromatin loops. *The Journal of Chemical Physics*, 132(4):044904, 2010.

S. Brown and G. Szamel. Structure and dynamics of ring polymers. *The Journal of Chemical Physics*, 108(12):4705–4708, 1998.

S. Brown, T. Lenczycki, and G. Szamel. Influence of topological constraints on the statics and dynamics of ring polymers. *Physical Review E*, 63(5):052801, 2001.

D. S. Callaway, M. E. J. Newman, S. H. Strogatz, and D. J. Watts. Network robustness and fragility: Percolation on random graphs. *Physical Review Letters*, 85(25):5468–5471, 2000.

M. E. Cates. Reptation of living polymers: Dynamics of entangled polymers in the presence of reversible chain-scission reactions. *Macromolecules*, 47(9):2289–2296, 1987.

M. E. Cates and J. M. Deutsch. Conjectures on the statistics of ring polymers. *Journal de Physique*, 47(12):2121–2128, 1986.

P. M. Chaikin and T. C. Lubensky. *Principles of Condensed Matter Physics*. Cambridge University Press, 2000.

S.-H. Chong and M. Fuchs. Mode-coupling theory for structural and conformational dynamics of polymer melts. *Physical Review Letters*, 88(18):185702, 2002.

N. Clauvelin, B. Audoly, and S. Neukirch. Elasticity and electrostatics of plectonemic DNA. *Biophysical Journal*, 96(9):3716–3723, 2009.

M. H. Cohen and D. Turnbull. Molecular transport in liquids and glasses. *The Journal of Chemical Physics*, 31(5):1164–1169, 1959.

J. P. Cotton. Polymer excluded volume exponent ν: An experimental verification of the n vector model for $n = 0$. *Journal de Physique Lettres*, 41(9):231–234, 1980.

J. M. G. Cowie and V. Arrighi. *Polymers: Chemistry and physics of modern materials, 3rd edition*. CRC Press Inc., 2008.

J. C. Crocker and B. D. Hoffman. Multiple-particle tracking and two-point microrheology in cells. *Methods in Cell Biology*, 83:141–178, 2007.

P.-G. de Gennes. Reptation of a polymer chain in the presence of fixed obstacles. *The Journal of Chemical Physics*, 55(2):572–579, 1971.

P.-G. de Gennes. *Scaling Concepts in Polymer Physics*. Cornell University Press, 1979.

J. des Cloizeaux. Ring polymers in solution: Topological effects. *Journal de Physique Lettres*, 42(19):433–436, 1981.

M. Doi and S. F. Edwards. *The Theory of Polymer Dynamics*. Oxford University Press, 1986.

P. S. Doyle, B. Ladoux, and J.-L. Viovy. Dynamics of a tethered polymer in shear flow. *Physical Review Letters*, 84(20):4769–4772, 2000.

J. C. Dyre. Colloquium: The glass transition and elastic models of glass-forming liquids. *Reviews of Modern Physics*, 78(3):953–972, 2006.

S. F. Edwards and P. W. Anderson. Theory of spin glasses. *Journal of Physics F: Metal Physics*, 5(5):965–974, 1975.

P. J. Flory. Molecular size distribution in three dimensional polymers. I. Gelation. *Journal of the American Chemical Society*, 63(11):3083–3090, 1941a.

P. J. Flory. Molecular size distribution in three dimensional polymers. III. Tetrafunctinoal branching units. *Journal of the American Chemical Society*, 63(11): 3096–3100, 1941b.

P. J. Flory. Molecular size distribution in three dimensional polymers. II. Trifunctional branching units. *Journal of the American Chemical Society*, 63(11):3091–3096, 1941c.

P. J. Flory. *Principles of Polymer Chemistry*. Cornell University Press, 1953.

S. Forth, C. Deufel, M. Y. Sheinin, B. Daniels, J. P. Sethna, and M. D. Wang. Abrupt buckling transition observed during the plectoneme formation of individual DNA molecules. *Physical Review Letters*, 100(14):148301, 2008.

A. Yu. Grosberg and A. R. Khokhlov. *Statistical Physics of Macromolecules*. AIP Press, 1994.

N. A. Grunina, T. V. Belopolskaya, and G. I. Tsereteli. The glass transition process in humid biopolymers. DSC study. *Journal of Physics: Conference Series*, 40: 105–110, 2006.

J. D. Halverson, W. B. Lee, G. S. Grest, A. Y. Grosberg, and K. Kremer. Molecular dynamics simulation study of nonconcatenated ring polymers in a melt. I. Statics. *The Journal of Chemical Physics*, 134(20):204904, 2011.

J. Z. Imbrie. Dimensional reduction and crossover to mean-field behavior for branched polymers. *Annales Henri Poincaré*, 4(1):445–458, 2003.

B. V. S. Iyer, A. K. Lele, and V. A. Juvekar. Flexible ring polymers in an obstacle environment: Molecular theory of linear viscoelasticity. *Physical Review E*, 74(2): 021805, 2006.

M. Kapnistos, M. Lang, D. Vlassopoulos, W. Pyckhout-Hintzen, D. Richter, D. Cho, T. Chang, and M. Rubinstein. Unexpected power-law stress relaxation of entangled ring polymers. *Nature Materials*, 7(12):997–1002, 2008.

A. R. Khokhlov and S. K. Nechaev. Polymer chain in an array of obstacles. *Physics Letters A*, 112(3-4):156–160, 1985.

J. Klein. Dynamics of entangled linear, branched, and cyclic polymers. *Macromolecules*, 19(1):105–118, 1986.

K. Kremer and G. S. Grest. Dynamics of entangled linear polymer melts: A molecular-dynamics simulation. *The Journal of Chemical Physics*, 92(8):5057–5086, 1990.

F. Lequeux. Repation of connected wormlike micelles. *Europhysics Letters*, 19(8): 675–681, 1992.

T. C. Lubensky and J. Isaacson. Field Theory for the Statistics of Branched Polymers, Gelation, and Vulcanization. *Physical Review Letters*, 41(12):829–832, 1978.

T. C. Lubensky and J. Isaacson. Statistics of lattice animals and dilute branched polymers. *Physical Review A*, 20(5):2130–2146, 1979.

J. F. Marko. Torque and dynamics of linking number relaxation in stretched supercoiled DNA. *Physical Review E*, 76(2):021926, 2007.

J. F. Marko and E. D. Siggia. Stretching DNA. *Macromolecules*, 28(26):8759–8770, 1995a.

J. F. Marko and E. D. Siggia. Statistical mechanics of supercoiled DNA. *Physical Review E*, 52(3):2912–2938, 1995b.

G. B. McKeena, B. J. Hostetter, N. Hadjichristidis, L. J. Fetters, and D. J. Plazek. A study of the linear viscoelstic properties of cyclic polystyrenes using creep and recovery measurements. *Macromolecules*, 22(4):1834–1852, 1989.

G. B. McKenna, G. Hadziioannou, P. Lutz, G. Hild, C. Strazielle, C. Straupe, P. Rempp, and A. J. Kovacs. Dilute solution characterization of cyclic polystyrene molecules and their zero-shear viscosity in the melt. *Macromolecules*, 20(3):498–512, 1987.

T. C. B. McLeish. Polymers without beginning or end. *Science*, 297(5589):2005–2006, 2002a.

T. C. B. McLeish. Tube theory of entangled polymer dynamics. *Advances in Physics*, 51(6):1379–1527, 2002b.

S. T. Milner and J. D. Newhall. Stress Relaxation in Entangled Melts of Unlinked Ring Polymers. *Physical Review Letters*, 105(20):208302, 2010.

M. Müller, J. P. Wittmer, and M. E. Cates. Topological effects in ring polymers: A computer simulation study. *Physical Review E*, 53(5):5063–5074, 1996.

M. Müller, J. P. Wittmer, and M. E. Cates. Topological effects in ring polymers. II. Influence of persistence length. *Physical Review E*, 61(4):4078–4089, 2000.

J. Norberg and L. Nilson. Glass transition in DNA from molecular dynamics simulations. *Proceedings of the National Academy of Sciences of the United States of America*, 93(19):10173–10176, 1996.

S. P. Obukhov, M. Rubinstein, and T. Duke. Dynamics of a Ring Polymer in a Gel. *Physical Review Letters*, 73(9):1263–1266, 1994.

D. J. Orrah, J. A. Semlyen, and S. B. Ross-Murphy. Studies of cyclic and linear poly(dimethylsiloxanes): 27. Bulk viscosities above the critical molar mass for entanglement. *Polymer*, 29(8):1452–1454, 1988.

G. Parisi and N. Sourlas. Critical Behavior of Branched Polymers and the Lee-Yang Edge Singularity. *Physical Review Letters*, 46(14):871–874, 1981.

R. M. Robertson and D. E. Smith. Strong effects of molecular topology on diffusion of entangled DNA molecules. *Proceedings of the National Academy of Sciences of the United States of America*, 104(12):4824–4827, 2007.

J. Roovers. The melt properties of ring polystyrenes. *Macromolecules*, 18(6):1359–1361, 1985.

J. Roovers. Viscoelastic properties of polybutadiene rings. *Macromolecules*, 21(5): 1517–1521, 1988.

A. Rosa, E. Orlandini, L. Tubiana, and C. Micheletti. Structure and dynamics of ring polymers: Entanglement effects because of solution density and ring topology. *Macromolecules*, 44(21):8668–8680, 2011.

M. Rubinstein. Dynamics of Ring Polymers in the Presence of Fixed Obstacles. *Physical Review Letters*, 57(24):3023–3026, 1986.

J. Sambrook, E. F. Fritsch, and T. Maniatis. *Molecular Cloning: A Laboratory Manual*. Cold Spring Harbor Laboratory Press, U.S., 1989.

K. S. Schweizer. Mode-coupling theory of the dynamics of polymer liquids: General formulation of a mode-coupling approach. *The Journal of Chemical Physics*, 91 (9):5802–58321, 1989a.

K. S. Schweizer. Mode-coupling theory of the dynamics of polymer liquids: Qualitative predictions for flexible chain and ring melts. *The Journal of Chemical Physics*, 91(9):5822–5839, 1989b.

D. E. Smith, T. T. Perkins, and S. Chu. Dynamical scaling of DNA diffusion coefficients. *Macromolecules*, 29(4):1372–1373, 1996.

A. P. Sokolov, H. Grimm, and R. Kahn. Glassy dynamics in DNA: Ruled by water of hydration? *The Journal of Chemical Physics*, 110(14):7053–7057, 1999.

D. Stauffer and A. Aharony. *Introduction to Percolation Theory, Second Edition*. Taylor & Francis Ltd, 1992.

W. H. Stockmayer. Theory of Molecular Size Distribution and Gel Formation in Branched-Chain Polymers. *The Journal of Chemical Physics*, 11(2):45–55, 1943.

W. H. Stockmayer. Theory of Molecular Size Distribution and Gel Formation in Branched Polymers II. General Cross Linking. *The Journal of Chemical Physics*, 12(4):125–131, 1944.

J. Suzuki, A. Takano, and Y. Matsushita. Topological effect in ring polymers investigated with Monte Carlo simulation. *The Journal of Chemical Physics*, 129(3): 034903, 2008.

J. Suzuki, A. Takano, T. Deguchi, and Y. Matsushita. Dimension of ring polymers in bulk studied by Monte-Carlo simulation and self-consistent theory. *The Journal of Chemical Physics*, 131(14):144902, 2009.

A. Takano. Ring polymers—Synthesis, characterization and the physical properties. *Polymer Prinprints, Japan*, 56:6, 2007.

D. T. Turner. Glass transition elevation by polymer entanglements. *Polymer*, 19 (7):789–796, 1978.

T. Vettorel, A. Y. Grosberg, and K. Kremer. Statistics of polymer rings in the melt: A numerical simulation study. *Physical Biology*, 6(2):25013, 2009.

B. H. Zimm and W. H. Stockmayer. The Dimensions of Chain Molecules Containing Branches and Rings. *The Journal of Chemical Physics*, 17(12):1301–1314, 1949.